Human Genomics

RESEARCH

Open Access

Development of oxidative stress- and ferroptosis-related prognostic signature in gastric cancer and identification of CDH19 as a novel biomarker

Shibo Wang[1†], Siyi Zhang[1†], Xiaoxuan Li[1], Chuanyu Leng[1], Xiangxue Li[1], Jing Lv[1], Shufen Zhao[1], Wensheng Qiu[1*] and Jing Guo[1*]

Abstract

Background Ferroptosis is a unique mode of cell death that is iron-dependent and associated with oxidative stress and lipid peroxidation. Oxidative stress and ferroptosis are essential mechanisms leading to metabolic abnormalities in cells and have been popular areas in cancer research.

Methods Initially, 76 oxidative stress and ferroptosis-related genes (OFRGs) were acquired by intersecting the gene sets from oxidative stress and ferroptosis. Afterwards, optimal OFRGs were screened using PPI networks, and individuals were separated into two OFRG subtypes (K = 2). Subsequently, we successfully constructed and verified a prognostic signature comprising SLC7A2, Cadherin 19 (CDH19), and CCN1. To further uncover potential biomarkers of gastric cancer (GC), we examined the expression level of CDH19, investigated the effects of knocking down CDH19 on the biological behavior of GC cells, and explored whether CDH19 is involved in ferroptosis and oxidative stress processes.

Results According to the findings, individuals in the low-risk scoring group have less infiltration of immune suppressive cells, fewer occurrences of immune escape and dysfunction, greater efficacy in chemotherapy and immunotherapy, and better survival outcomes. The qRT-PCR assay indicated that CDH19 expression was significantly higher in GC cells. Through experiments, we demonstrated that knocking down CDH19 can affect the transcription levels of ACSL4 and GPX4, increase intracellular iron ion concentration and accumulation of reactive oxygen species (ROS), and inhibit the proliferation and migration of GC cells.

Conclusion We developed an OFRG-related signature to predict the prognosis and treatment responsiveness of individuals with GC and identified CDH19 as a possible therapeutic target for GC.

[†]Shibo Wang and Siyi Zhang contributed equally to this work.

*Correspondence:
Wensheng Qiu
wsqiuqdfy@qdu.edu.cn
Jing Guo
guojing-melody@163.com

Full list of author information is available at the end of the article

Keywords Immunotherapy ferroptosis, Oxidative stress, CDH19, Prognostic biomarker

Introduction

Gastric cancer (GC) is one of the most widespread digestive tract tumors. Global cancer statistics for 2024 show that there will be almost 20 million new cases of cancer worldwide, with 968,784 instances 4.9%) being GC. Nearly 9.6 million cancer patients died, and 660,175 (6.8%) of them had GC. In terms of both incidence and mortality, GC was placed fifth among malignant tumors [1]. In addition, there are apparent regional variations in the incidence rate of GC. Its incidence rate in Asia (especially China and Japan) is significantly higher than in other countries and areas [2], posing a severe threat to public health. The pathogenesis of GC is multifaceted, multistep, and multistage. The most notable risk factor is Helicobacter pylori infection [3]. Early GC can be treated with endoscopy or radical surgery and generally have a better prognosis. However, most patients are diagnosed when the disease has advanced, and there is a substantial risk of distant metastasis and local recurrence [4]. In recent years, the application of targeted medications (such as trastuzumab) and immune checkpoint inhibitors (ICIs; anti-PD-1, anti-PD-L1, and anti-CTLA4) has benefited the clinical outcomes of some GC patients [5]. Nevertheless, immunotherapy is still limited for most people. Therefore, exploring more biomarkers and seeking novel therapeutic targets for GC is imperative.

Ferroptosis was initially proposed in 2012 as a multilevel regulatable iron-dependent lipid peroxidation-driven cell death process [6]. Ferroptosis differs from other cell death modes in morphology and mechanism, such as apoptosis, autophagy, and necrosis. Morphologically, cells that undergo ferroptosis typically exhibit loss of plasma membrane integrity, mitochondrial shrinkage, and increased mitochondrial membrane density [7]. Ferroptosis is characterized by two primary features: iron accumulation and redox imbalance. Ferroptosis inducers, such as Erastin and RSL3, increase intracellular iron accumulation, which generates excess reactive oxygen species (ROS) through the Fenton reaction, thereby exacerbating cellular oxidative damage [8, 9]. Moreover, iron may increase the activity of lipoxygenases (LOXs) or cytochrome P450 reductase (PORs), which regulate lipid peroxidation and oxygen homeostasis. The second hallmark of ferroptosis is redox imbalance. LOXs and PORs elevate levels of phospholipid hydroperoxides (PLOOHs), which encourage polyunsaturated fatty acid (PUFA) peroxidation in the cell membrane. This peroxidation process leads to the destruction of cellular and organelle membranes, ultimately resulting in cell death [10, 11]. Consequently, ferroptosis can be inhibited by antioxidants and iron chelators.

In addition, ferroptosis has been proven to play a crucial role in inhibiting tumor cell proliferation and overcoming drug resistance in hepatocellular carcinoma, breast cancer, lung cancer, and other cancers [12–14]. On the one hand, various classic cancer treatment strategies can trigger ferroptosis. On the other hand, ferroptosis is influenced by cellular metabolism, including mitochondrial activity and lipid metabolism, as well as cancer signaling pathways such as AMPK, E-cadherin-NF2 Hippo YAP, and HIF2α- HILPDA pathways [15–17]. However, tumor cells can also develop resistance to ferroptosis and promote cancer progression through specific mechanisms, including limiting the synthesis and peroxidation of PUFA-PL, reducing unstable iron supply, and upregulating the cellular defense system to combat ferroptosis [6].

Oxidative stress is a state of imbalance between oxidation and antioxidants in the body, with lipid peroxidation serving as the fundamental mechanism of ferroptosis. Oxidative stress can produce excessive oxidation intermediates like ROS and reactive nitrogen species (RNS), which can directly or indirectly damage DNA, proteins, and lipids, induce gene mutation, and cause cell or tissue damage [18]. These intermediates are significant risk factors for human aging and various illnesses, including cancer, cardiovascular disease, and diabetes. In recent years, oxidative stress in cancer has garnered considerable attention. Tumor cells can increase NADPH level by activating AMPK, pentose phosphate pathway (PPP), and reducing glutamine and folate metabolism. Additionally, they can alter the activity of sulfur metabolism and antioxidant transcription factors to survive under high ROS levels [19]. Prior research has indicated that patients with thyroid, breast, and gastric cancers exhibit significantly higher levels of oxidative stress than normal individuals, while the level of antioxidant enzymes is significantly lower [20–22]. Although oxidative stress may foster tumor formation and proliferation, excessive ROS also possess cytotoxic properties that can lead to tumor cell death and limit cancer metastasis [23].

In conclusion, oxidative stress and ferroptosis constitute crucial factors in the onset and progression of cancer. Despite integrated studies on oxidative stress and ferroptosis in GC remain scarce, combined studies on oxidative stress and ferroptosis in GC are still lacking. Thereby, using public databases related to GC for bioinformatics analysis, this paper assesses oxidative stress and ferroptosis subtypes and connects them to the characteristics of immune infiltration. Subsequently, a signature model related to oxidative stress and ferroptosis-related genes (OFRGs) was constructed through differential analysis

and Cox analysis to predict patient prognosis and treatment response, explore the pathogenesis of oxidative stress and ferroptosis in GC, reveal the immune landscape, and identify new potential biomarkers.

Materials and methods

Data collection

We downloaded RNA-sequencing, somatic mutation, and clinical data from The Cancer Genome Atlas (TCGA) database (https://portal.gdc.cancer.gov/) and the Gene Expression Omnibus (GEO) database (https://www.ncbi.nlm.nih.gov/). The screening criteria for genes require expression in at least 50% of the samples. The TCGA-STAD queue consists of 36 normal gastric samples and 410 GC samples, of which 414 samples have prognostic information. GSE54129 queue has 21 normal gastric samples and 111 GC samples. GSE84437 and GSE62254 cohorts contain expression information and prognostic data for 433 and 300 individuals with GC, respectively. Expression data (TPM) of 174 normal gastric tissue samples acquired from GTEx database (https://www.gtexportal.org). The copy number variation (CNV) and RNA stemness scores (RNAss) were attained from the UCSC Xena database (https://xenabrowser.net/datapages/). Immunotherapy data are downloaded from The Cancer Immunome Atlas (TCIA, https://tcia.at/patients). 566 oxidative stress-related genes (ORGs) were obtained from the Molecular Signatures Database (MisDB) website (http://www.gsea-msigdb.org/gsea/msigdb/index.jsp), and 484 ferroptosis-related genes (FRGs) were acquired from the FerrDb website (http://www.zhounan.org/ferrdb/current/). The detailed gene sets are shown in Table S1.

Identification of oxidative stress- and ferroptosis-related genes (OFRGs)

We obtained OFRGs by intersecting ORGs and FRGs and then analyzed these genes using Gene Ontology (GO) and the Kyoto Encyclopedia of Genes and Genomes (KEGG) [24, 25]. We subsequently analyzed somatic mutations and plotted waterfall plots related to OFRGs. Based on the copy number of genes in all samples in the TCGA-STAD database, the copy number variation (CNV) frequency of OFRGs was calculated and use the a circular graph was generated using the "Rcircos" package [26]. The Wilcoxon test and "limma" package [27] were used to compare the expression of OFRGs in normal and GC tissues. Survival curves for prognosis-related OFRGs were plotted through univariate Cox analysis and Kaplan-Meier (K-M) method.

Consensus clustering to determine OFRG subtypes

Initially, we established a Protein-Protein Interaction (PPI) network for OFRGs using STRING (https://cn.string-db.org/) and imported it into Cytoscape software. Then, we applied the "ConsonsusClusterPlus" package [28] to perform consensus clustering analysis in GC individuals and classified them according to the optimal value of the cumulative distribution function (CDF) curve. The R packages "ggplot2" and "Rtsne" were employed for principal component analysis (PCA) and t-distributed stochastic neighbor embedding (t-SNE) analysis, respectively. We exploited K-M curves to plot the overall survival (OS) and performed molecular functional and pathway analysis between clusters through GO, KEGG, and gene set variation analysis (GSVA) [29]. Single sample gene set enrichment analysis (ssGSEA) was utilized to detect the abundance of immune cell infiltration between two clusters.

Construction and verification of prognostic signatures for OFRGs

The differentially expressed genes (DEGs) between two OFRGs clusters are determined using the "limma" packages. The criteria for DEGs are | logFC | > 1 and FDR < 0.05. Univariate Cox analysis was performed on these DEGs to categorize GC individuals into distinct gene clusters (K=2). Subsequently, the predictive signature model was further developed using the Least Absolute Shrinkage and Selection Operator (LASSO) and multivariate Cox analyses. Risk scores were calculated based on gene expression and coefficients, allowing for the stratification of GC patients into high- and low-risk subgroups. This model was validated using the GSE84437 cohort. The following formula was employed to compute the risk score:

$$\text{Risk score} = \sum_{i=1}^{n} (\text{Coefi} * \text{Expi})$$

Coefi is gene coefficient; Expi is gene expression; n is the number of genes in signature.

The relationship between OFRGs subtype, gene cluster, and risk signature was investigated through the Sankey diagram [30]. Researchers conducted enrichment analysis on high- and low-risk categories using GSVA and utilized K-M curves to compare survival outcomes. Cox analysis was employed to identify independent prognostic factors for GC and develop a nomogram [31] based on risk scores and additional clinicopathological features. Calibration curves for 1-, 3-, and 5-year were generated to validate accuracy, and the sensitivity and specificity of risk signature and nomogram were estimated using the ROC curves [32]. Additionally, we also probed the correlation between risk scores and clinicopathological parameters and forecasted patient survival outcomes in various clinical pathology subgroups.

Analyzing the immune cell infiltration and immunotherapy

With the ESTIMATE algorithm [33], we assessed the immune, stromal, and estimated scores in the tumor microenvironment (TME) of GC patients and then performed immune function analysis in the high- and low-risk subgroups. Multiple algorithms, including ssGSEA, Xcell, Timer, Cibersort, and others, were employed to measure the degree of infiltration of tumor-infiltrating immune cells (TIICs) in the risk categories [34]. The expression levels of a few recognized immune checkpoints and RNAss were compared between the risk subgroups via the Wilcoxon test. The Tumor Immune Dysfunction and Exclusion (TIDE) score (http://tide.dfci.harvard.edu/) was employed to evaluate immune escape and immune dysfunction in patients with GC. A higher TIDE score indicates a greater likelihood of immune escape and reduced benefits from immunotherapy.

Moreover, we retrieved microsatellite (MS) status and ICI treatment data from the TCIA website, split all GC individuals into microsatellite stable (MSS), low-level microsatellite instability (MSI-L), and high-level microsatellite instability (MSI-H) subgroups, and predicted the efficacy of anti-CTLA-4 and anti-PD-1 medication for those in high and low-risk subgroups. We explored the association between risk score and tumor mutation burden (TMB) using the "ggpubr" package. Then, the "survival" and " survminer " packages [35] were applied to execute a combined survival analysis for the high and low TMB score, risk score, and Cadherin 19 (CDH19) expression groups. Ultimately, we forecasted drug sensitivity in high and low-risk subgroups utilizing the "oncoPredict" package [36].

Identifying CDH19 as a potential biomarker for GC

The researchers analyzed the expression of CDH19 in GC and evaluated expression differences using qRT-PCR. Then, we employed GSEA for functional and pathway enrichment analysis and investigated the association between CDH19 and clinical outcome indicators such as progression free survival (PFS) and disease-free survival (DFS). We utilized ssGSEA to analyze the infiltration abundance of TIICs in the high and low CDH19 groups. Further, this study also predicted the efficacy of immunotherapy based on the expression of CDH19.

Cell culture and reagents

Human gastric epithelial cells (GES-1) and Human GC cell lines (AGS, HGC27, and MKN-7) were obtained from the Chinese Academy of Sciences Cell Bank (Shanghai, China) type culture bank. These cell lines were identified by STR and tested negative for mycoplasma. These cell lines were cultured in Losvi-Parker Memorial Institute (RPMI)-1640 medium (HyClone, USA) supplemented with 10% fetal bovine serum (FBS) (HyClone, USA), 100 U/mL penicillin (HyClone, USA), and 100 μg/mL streptomycin (HyClone, USA) at 37 °C, 5% CO2.

Lentiviral transfection

The RNAi lentivirus vector was constructed by the Gikai gene (http://www.genechem.com.cn/). The targ et lentiviral vector used was GV493, with the element sequence hU6-MCS-CBh-gcGFP-IRES-puromycin (Reference number: CON313). The RNAi negative control (sh-NC) sequence was TTCTCCGAACGTGTCACG T. The shRNA sequences designed for CDH19 were as follows: sh-CDH19-1: CCACTGTATGTGCAAGTTC TT. sh-CDH19-2: CGATCCCTCAAGTGGTAATAA. Sh-CDH19-3: CCCAGGTAATAGACATCGCTA. AGS and HGC-27 cell lines were inoculated in 6-well plates at a density of 2×10^4 cells per well. After 24 h of incubation, the medium was replaced, and the diluted virus solution was added. After 24 h of infection, the cells were moved to a cell culture dish, and puromycin was added for screening (48 h, repeated three times) to obtain stable transfection. The two most significantly knock-down cell lines from AGS and HGC-27 cells successfully transfected with lentivirus were then selected.

Quantitative real-time polymerase chain reaction (qRT-PCR)

Total RNA was extracted from cells utilizing TRIzol® reagent and reversely transcribed it into cDNA. In the qRT-PCR process, the reaction mixture consisted of 2 μl of reverse transcription product, 7.2 μl of DEPC, 10 μl of SYBR, and 0.4 μl of forward and reverse primer. The qRT-PCR reactions were performed under the following conditions: Pre-denaturation at 95 °C for 30 s, followed by 40 cycles of 95 °C for 10 s and 60 °C 30 s. Finally, the melting curve analysis was conducted with the following steps: 95 °C for 15 s, 60 °C for 60 s, and 95 °C for 15 s. The primer sequences are as follows:

CDH19-F (5′-AGTCATCACATCGGCCAGCTAAG A-3′).

CDH19-R (5′-TACTTCCAGCTCCAGCTCCCAA A-3′).

β-actin F (5'-GACCACCTTCAACTCCATCAT-3').

β-actin R (5'-CCTGCTTGCTAATCCACATCT-3').

β-actin was used as the internal reference, and the $2-\Delta\Delta Ct$ method was applied to determine the expression level of CDH19. The experiment was repeated three times.

Cell viability assay MTT

GC cells transfected with sh-NC or sh-CDH19 lentivirus were inoculated into 96-well plates at a density of 7×103/well. After cell culture, 500 μL of 0.5 mg/mL MTT solution prepared with FBS-free medium was added to each well and incubated in the incubator for at least two hours.

The resulting blue-violet crystal formazeris was then melted with equivalent DMSO. Absorbance at 490 nm was measured using a full-featured microplate detector (BioTek, USA), and cell viability was calculated as follows: cells (%) = OD of experimental group/OD of control group. Cell proliferation was monitored every 24 h for a period of 3 days to evaluate cell proliferation. All data were processed in Excel and imported into GraphPad Prism 9 software for graphical drawing.

Migration assays

GC cells transfected with sh-NC or sh-BCHE lentivirus were seeded in 6-well plates and stable cell cultures. When the cell density exceeds 90% of the area of each well, a 200 μL tip was used to create a wound on the cell surface. After washing the floating cells with phosphate-buffered saline (PBS), the adherent cells were grown in a culture medium for 4 h. The images were obtained at 0 and 48 h. The scratch area was measured three times to evaluate the cell healing rate. The data were analyzed using ImageJ software and graphs were generated using GraphPad Prism 9 software.

Colony formation assay

AGS and HGC-27 cells, transfected with sh-NC or sh-CDH19, were seeded in 6-well plates at a density of 1000 cells per well. The cells were cultured in RMPI-1640 medium containing 10% fetal bovine serum, with the medium being refreshed every two days. Incubation was carried out in a CO2 incubator maintained at 37 °C with 5% CO2. After 14 days, cell colonies were fixed in 4% paraformaldehyde at room temperature, stained with crystal violet, and subsequently photographed.

Western blot analysis

Cells were lysed using IP buffer, and the supernatant was collected using a centrifuge. Proteins were separated with 10% SDS-PAGE (20 μg/sample) and transferred to PVDF membranes (Millipore, Billerica, and MA, USA). The membranes were blocked with 5% skim milk for 1 h and then incubated overnight with the primary antibody at 4 °C. Following three washes with wash buffer (10 min per wash), the membranes were incubated with the secondary antibody for 1 h at 37 °C. After an additional three washes with wash buffer (10 min per wash), the membranes were developed. The experiment was repeated three times. The antibodies used were glutathione peroxidase 4 (GPX4; Abcam, USA), SLC7A11, ACSL4, and GAPDH (Proteintech, China).

ROS assay

In RPMI-1640 medium without FBS, the ROS assay H2DCFDA (10 mmol/L) and DHE (10 mmol/L) were diluted to a final concentration of 10 μmol/L, and then the prepared DCFH-DA and DHE were added to the cell plate and incubated with the cells for 40 min, then aspirated and added DAPI for 15 min, and the ROS level was measured by fluorescence inverted microscopy. The images were merged using imagej software, and all experiments were repeated three times.

Iron staining

Dilute 1 mmol/L of FerroOrange (Dojindo, China) to a final concentration of 1 μmol/L in HBSS solution, then add the prepared FerroOrange to the cell plate and incubate with the cells for 30 min before fluorescence inverted microscopy to measure Fe2+levels.

Statistic nalysis

R software (Version 4.2.2, http://www.R-project.org) and GraphPad Prism (Version 9.3.1, CA, USA) were employed to perform statistical analyses. Wilcoxon test was applied for intergroup comparative, and Spearman was utilized for correlation analysis. Kaplan-Meier curves were implemented for survival analysis. Consensus clustering analysis was used for OFRG and gene clusters. The "timeROC" and "survival" packages were conducted for the ROC curve and Cox regression analysis. $P<0.05$ was considered statistically significant (ns: $p>0.05$; $^{*}P\leq0.05$; $^{**}P\leq0.01$; $^{***}P\leq0.001$; ****, $P<0.0001$).

Results

Identifying prognostic genes related to oxidative stress and Ferroptosis

Following the intersection of 566 ORGs and 484 FRGs, 76 OFRGs were identified in total (Fig. 1A), and enrichment analyses were performed on these genes. GO analysis showed that they were primarily enriched in the "response to oxidative stress" of biological process (BP), the "NADPH oxidation complex" and "oxidoreductase complex" of cellular component (CC), and the "superoxide generating NAD (P) H oxidation activity" and "antioxidant activity" of molecular function (MF). According to KEGG analysis, these genes were associated with the "Chemical cancer genes reactive oxygen species" and "TNF signaling pathway" (Fig. 1B). Gene mutation analysis of OFRGs revealed that TP53 exhibited the highest mutation frequency, and missense mutation was the most prevalent type of mutation. A waterfall plot was created using the top 20 genes with the highest frequency of mutations (Fig. 1C).

Additionally, we examined the CNV levels of OFRGs and observed that GAIN variation occurred more frequently than LOSS variation. We also created a copy number circle diagram representing these genes' chromosomal locations (Fig. 1D, E). Through univariate COX analysis, 15 prognostic-related OFRGs were determined (Fig. 1F), with their K-M survival curves displayed in

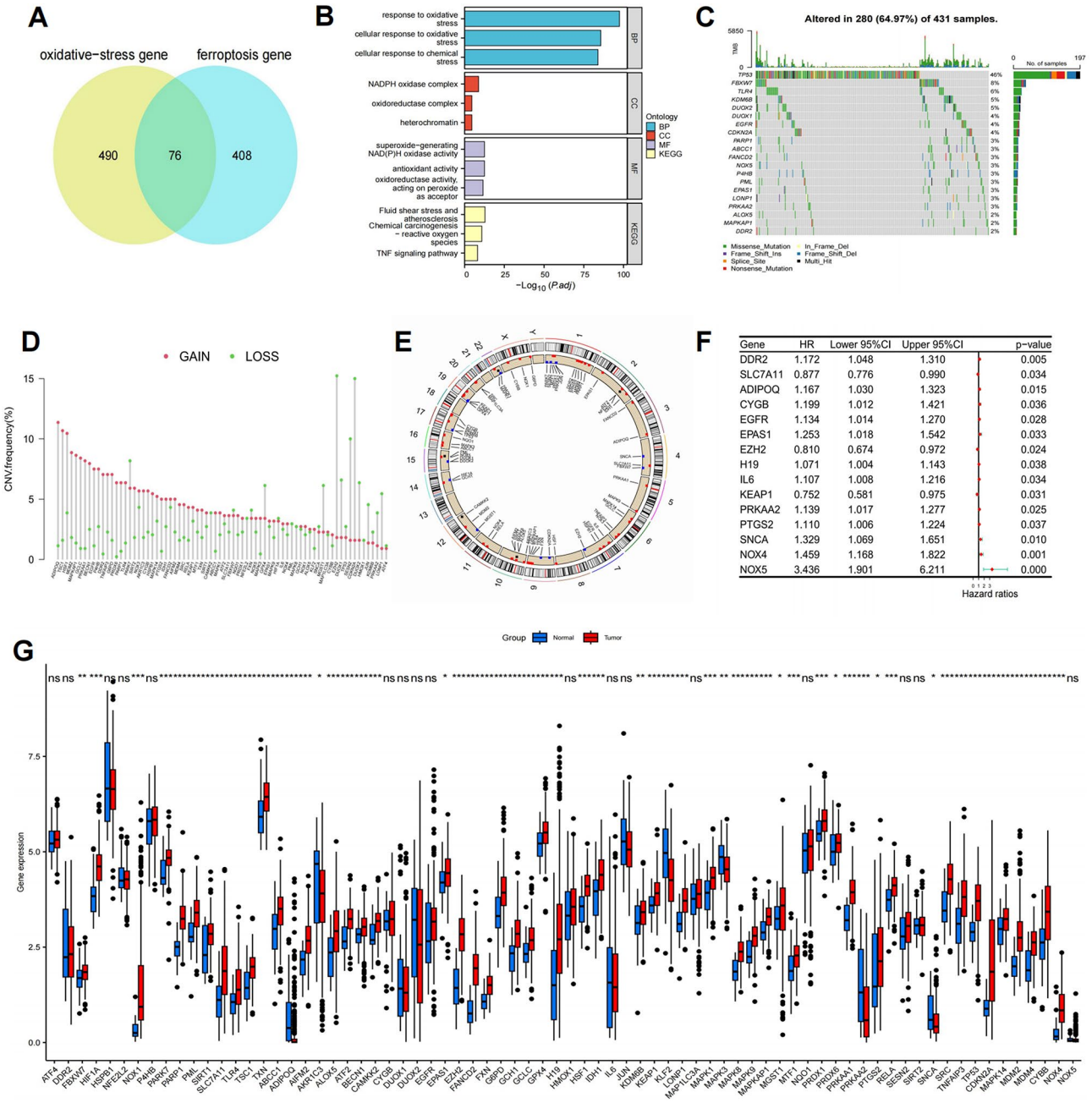

Fig. 1 Genetic, expression, and mechanism analysis of OFRGs in gastric cancer. (**A**) Determine 76 OFRGs through Veen diagram. **(B)** GO and KEGG analyses of OFRGs. **(C)** The mutation state of OFRGs in somatic cells. **(D)** The frequency of CNVs gain and loss in OFRGs. **(E)** Locations of CNV alterations in OFRGs on chromosomes. **(F)** Determine OFRG associated with prognosis through univariate Cox analysis. **(G)** The expression of OFRGs in normal gastric samples and gastric cancer samples in the TCGA database. ns $p > 0.5$; *$p < 0.05$; **$p < 0.01$; ***$p < 0.001$. OFRGs, oxidative stress and ferroptosis-related genes; GO, Gene Ontology; KEGG, Kyoto Encyclopedia of Genes and Genomes; CNV, copy number variation; TCGA, The Cancer Genome Atlas

Figure S1. Subsequent differential analysis of tumor and adjacent samples from the TCGA cohort revealed significant differences in the expression of the majority of OFRGs (Fig. 1G).

Consensus clustering analysis

The researchers used the STRING website to generate a PPI network of OFRGs and imported Cytoscape software to screen out the five most critical OFRGs (Fig. 2A). Consensus clustering analysis was performed, dividing all GC samples into two OFRG clusters (K=2) (Fig. 2B, Table S2). PCA and t-SNE demonstrated significant dispersion

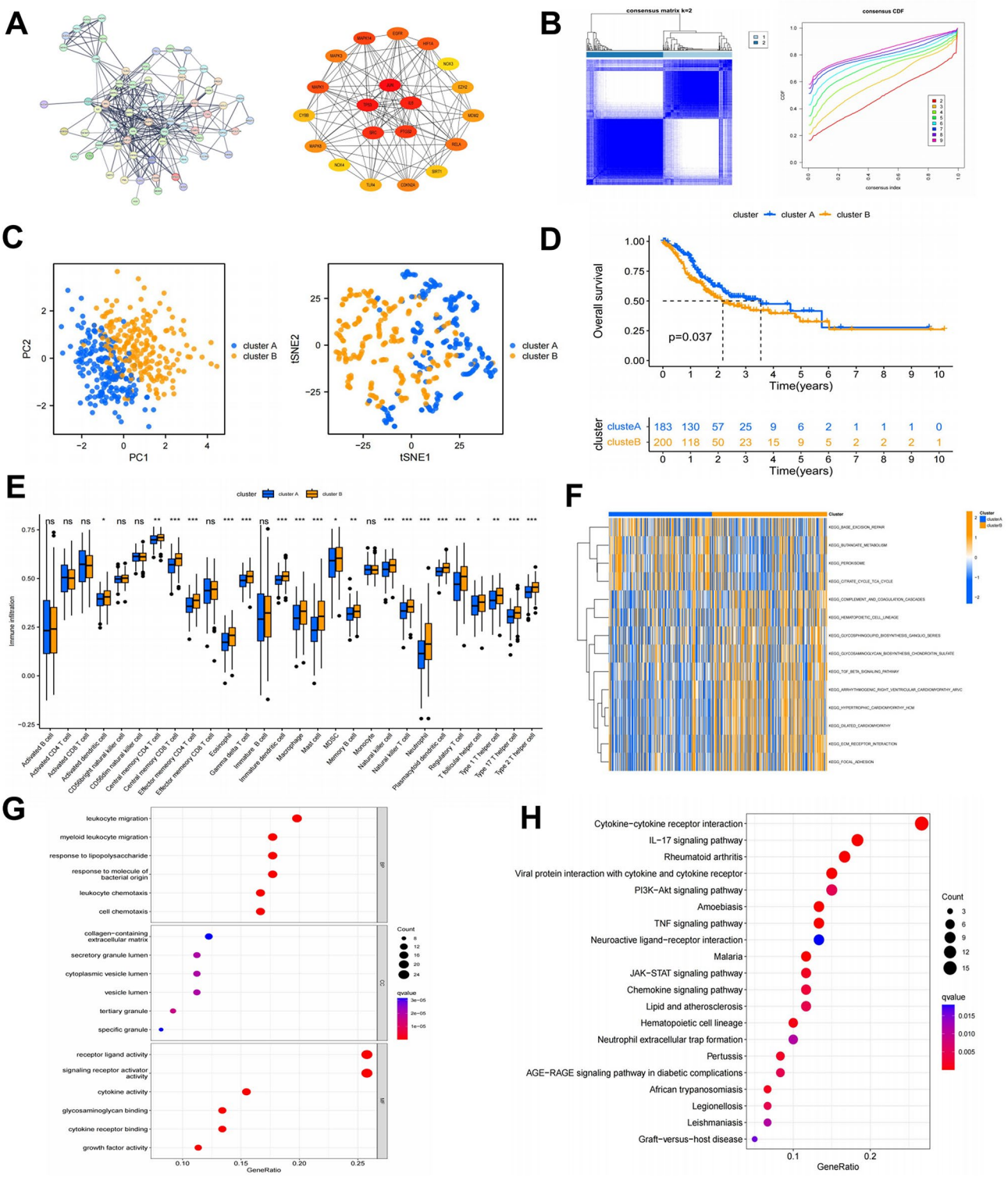

Fig. 2 Consensus clustering analysis. (**A**) PPI network of OFRGs constructed utilized STRING website and Cytoscape software. **(B)** Consensus clustering analysis based on OFRGs. **(C)** PCA and t-SNE analysis of OFRG clusters. **(D)** K-M analysis of OFRG clusters. **(E)** Evaluate the level of immune cell infiltration through the ssGSEA algorithm. **(F)** GSVA analysis of OFRG clusters. **(G**, **H)** GO and KEGG analysis of DEGs between OFRG clusters. ns $p > 0.5$; *$p < 0.05$; **$p < 0.01$; ***$p < 0.001$. PPI, Protein-Protein Interaction; OFRGs, oxidative stress and ferroptosis-related genes; PCA, principal component analysis; t-SNE, t-distributed stochastic neighbor embedding; K-M, Kaplan-Meier; ssGSEA, single sample gene set enrichment analysis; GSVA, gene set variation analysis; DEGs, differentially expressed genes

between the two clusters, which is helpful for distinguishing patients (Fig. 2C). Furthermore, a statistically significant distinction in survival outcomes was observed between the two patient groups ($p<0.05$), with patients in cluster A showing a more prolonged OS(Fig. 2D). We used the ssGSEA approach to measure the expression levels of immune cells in two clusters. We identified significant differences in 20 different types of immune cells, with cluster B displaying higher immune-suppressive cell infiltration (Fig. 2E). Subsequently, we employed GSVA analysis to generate a heat map of the KEGG pathway between the two clusters. The enrichment pathways of cluster A, namely "BASE_EXCISION_REPAIR", "PEROXISOME", and "CITRATECYCLE_TCA_CYCLE", primarily focus on cellular function and metabolism. The pathways enriched in cluster B, such as "TGF_BETASIGNALING_PATHWAY" and "FOCAL_ADHENSION," are linked to matrix and cancer activation (Fig. 2F). Subsequently, we conducted differential analysis on clusters A and B (| logFC |>1.0 and FDR<0.05) and performed enrichment analysis on DEGs. The GO analysis implied that these DEGs were primarily enriched in pathways, including "Leukocyte migration", "myeloid Leukocyte migration", and "response to lipopolysaccharide" (Fig. 2G). According to KEGG findings, DEGs were associated with pathways that promote inflammation and carcinogenesis, such as the "IL-17 signaling pathway" and the "PI3K-Akt signaling pathway" (Fig. 2H).

Construction and validation of a prognostic risk signature

Upon identifying prognostic-related genes by univariate COX analysis on the aforementioned DEGs (Fig. 3A), we categorized all GC samples into gene clusters A or B (K=2) using clustering analysis (Fig. 3B, Table S1). Expression levels of JUN, IL6, and PTGS2 were lower in gene cluster B, whereas SRC expression was elevated. TP53 did not significantly change between the two gene clusters (Fig. 3C). In addition, the K-M curve indicated that patients in gene cluster B had a superior prognosis (Fig. 3D). Then, we performed LASSO analysis to mitigate the risk of overfitting and ultimately constructed a prognostic signature for OFRGs, including SLC7A2, CDH19, and CCN1, through multivariate analysis (Fig. 3E, F). The risk score for each sample was calculated as follows: Risk score= (0.128282677879963) × SLC7A2 expression + (0.13087784597397) × CDH19 expression + (0.120683245893589) × CCN1 expression. GC patients were classified as high-risk or low-risk groups based on the median risk score. Table S4 displays the results of the risk score. Notably, the high-risk group exhibited elevated expression levels of SLC7A2, CDH19, and CCN1 (Fig. 3G). Furthermore, K-M analysis revealed that the groups with higher expression levels of these three genes had worse prognostic outcomes and a shorter OS period (Fig. 3H). Afterward, we generated a Sankey plot of OFRG clustering, gene clustering, risk signature, and survival outcomes (Fig. 4A). Figure 4B and C illustrated that the risk scores of cluster B and gene cluster A groups were significantly higher, supporting the consistency and reliability of the previous analysis. K-M analysis indicated that the OS of high-risk scoring populations in the TCGA and GSE84437 cohorts was significantly shorter (Figs. 4D and 5A), and the scatter plot of risk scores and patient survival statistics also demonstrated that patients with higher risk scores had a higher risk of death (Figs. 4E and 5B). The ROC curve displayed area under curve (AUC) values of 0.631, 0.637, and 0.652 for 1, 3, and 5 years, respectively. Compared to other clinical features, the risk signature has the highest 5-year AUC value (Fig. 4F), and consistent results were shown in the GSE84437 cohort (5 C). Through PCA method dimensionality reduction analysis, we found that the high and low-risk groups exhibited two distinct development trend directions with good dispersion, suggesting that the risk score can effectively differentiate GC patients (Fig. 4G).

In addition, to further evaluate the significance of risk score in predicting the prognosis of GC patients, we carried out COX regression analysis on risk score and several clinical characteristics, including age, gender, grade, and stage. Univariate Cox analysis displayed that Age (HR=1.022, 95% CI=1.006–1.039, $p<0.01$), Stage (HR=1.596, 95% CI=1.294–1.970, $p<0.001$), and Risk score (HR=1.685, 95% CI=1.339–2.120, $p<0.001$) can significantly affect the OS of GC. In multivariate Cox analysis, Age (HR=1.032, 95% CI=1.015–1.050, $p<0.001$), Stage (HR=1.676, 95% CI=1.346–2.087, $p<0.001$), and Risk score (HR=1.717, 95% CI=1.353–2.180, $p<0.001$) were independent prognostic factors. Cox regression analysis of univariate (HR=3.261, 95% CI=1.521–6.997, $p=0.002$) and multivariate (HR=3.812, 95% CI=1.761–8.253, $p<0.001$) in the GSE84437 cohort also confirmed the best predictive effect of risk score (Fig. 5D). Later, we conducted mechanistic analysis on the high and low-risk groups using GSVA, suggesting that the low-risk group's enriched pathways were primarily related to cellular metabolism and function. In contrast, the high-risk group was linked to signaling pathways associated with cancer occurrence and development, such as "TGF_BETA," "HEDGELOG," "MTOR," and "MAPK," as well as the matrix secretion and activation pathways like "FOCAL_ADHESION" and "GAP_JUNCTION" (Fig. 5E).

Establishment and evaluation of a nomogram

In order to predict GC individuals' survival time and survival rate, researchers constructed a clinical nomogram combining clinical pathological features and risk scores (Fig. 5F, Table S5). For instance, the nomogram predicts

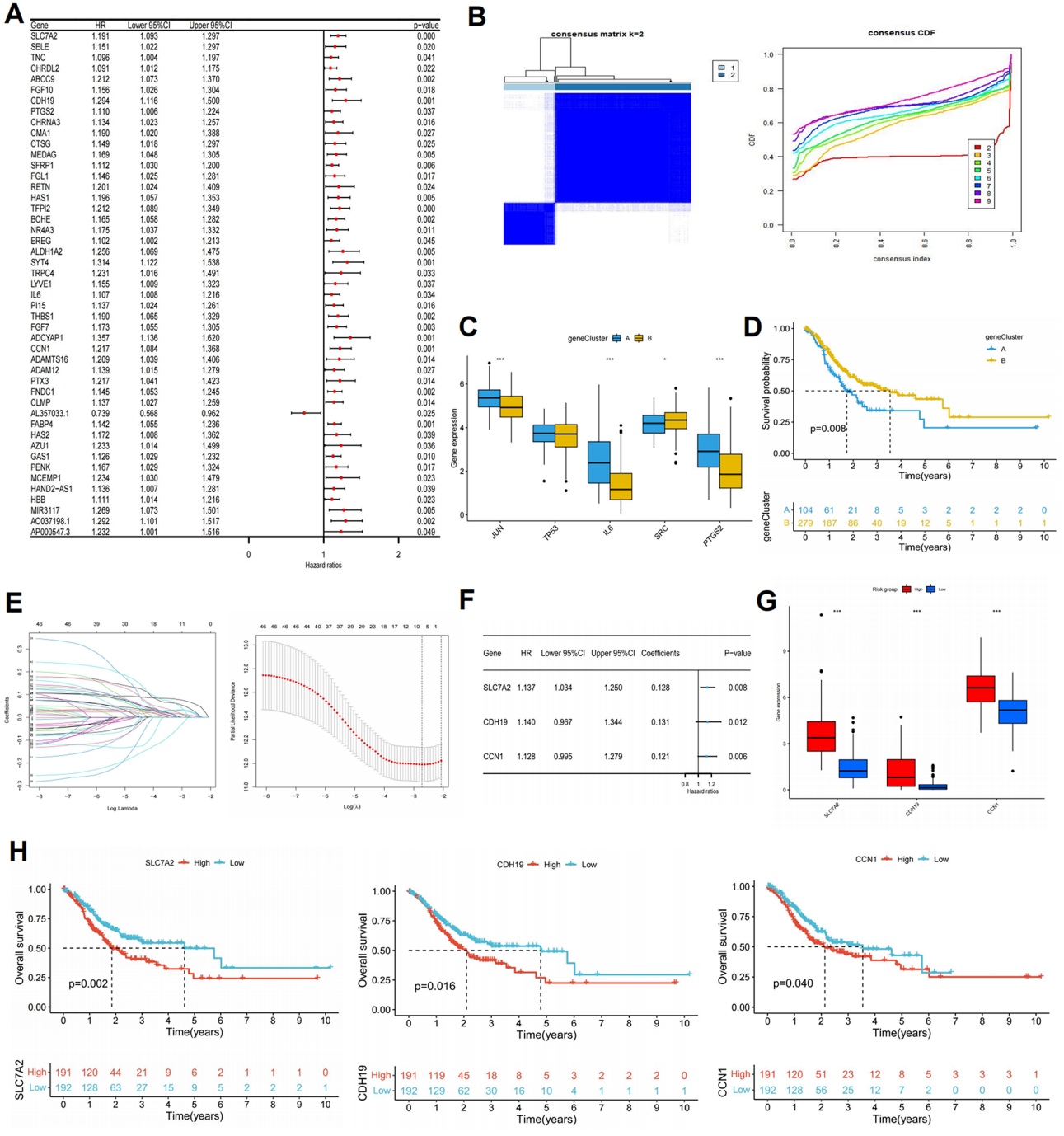

Fig. 3 Development of a prognostic risk signature for OFRGs. (**A**) Genes associated with prognosis in DEGs of clusters **A** and **B**. **(B)** Divide gene clusters based on consensus clustering analysis. **(C**, **D)** Expression and prognostic analysis of gene clusters. **(E)** Lasso Cox regression analysis and cross-validation. **(F)** Multivariate Cox analysis for determining the optimum signature genes. **(G)** Expression of signature genes in high and low-risk subgroups. **(H)** K-M analysis of signature genes in the risk signature. *$p < 0.05$; **$p < 0.01$; ***$p < 0.001$. OFRGs, oxidative stress and ferroptosis-related genes; DEGs, differentially expressed genes; LASSO, Least Absolute Shrinkage and Selection Operator; K-M, Kaplan-Meier

a patient's 1-year, 3-year, and 5-year survival rates to be 62.1%, 23.8%, and 13.6%, respectively, with a total score of 159. The C-index value of calibration curve and AUC of the ROC curve for years 1, 3, and 5 of the nomograms were all greater than 0.65, confirming the accuracy of the prediction capacity of the nomogram. Moreover, we examined the correlations between the risk score and the clinical pathological features of GC, discovering that higher grades, later T stages, and death populations all had considerably higher risk scores (Figure S2 A-H).

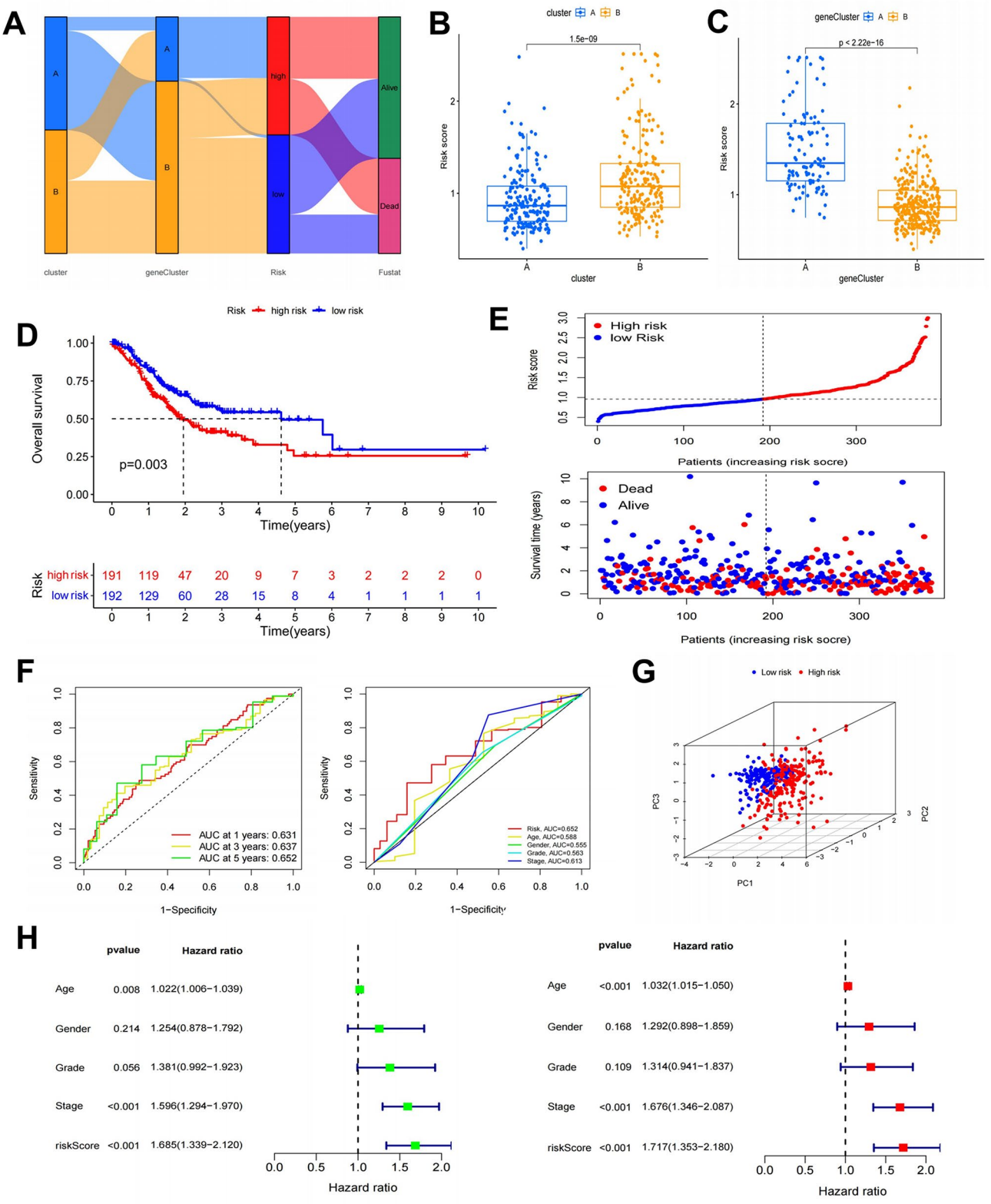

Fig. 4 Evaluation of the risk signature. (**A**) Sankey plot between OFRG clusters, gene clusters, risk signature, and GC prognosis. **(B)** The relationship between OFRG clusters and risk scores. **(C)** The relationship between gene clusters and risk scores. **(D)** K-M analysis of the risk signature in the TCGA-STAD queue. **(E)** Distributions of risk scores and survival statuses. **(F)** ROC curve for the risk signature and other clinical characteristics. **(G)** PCA between risk subgroups based on the OFRGs signature. **(H)** Cox regression analyses of the signature and other clinical parameters in the TCGA cohort. OFRGs, oxidative stress and ferroptosis-related genes; GC, gastric cancer; K-M, Kaplan-Meier; ROC, receiver operating characteristics curve; PCA, principal component analysis. OFRGs, oxidative stress and ferroptosis-related genes; GC, gastric cancer; K-M, Kaplan-Meier; TCGA, The Cancer Genome Atlas

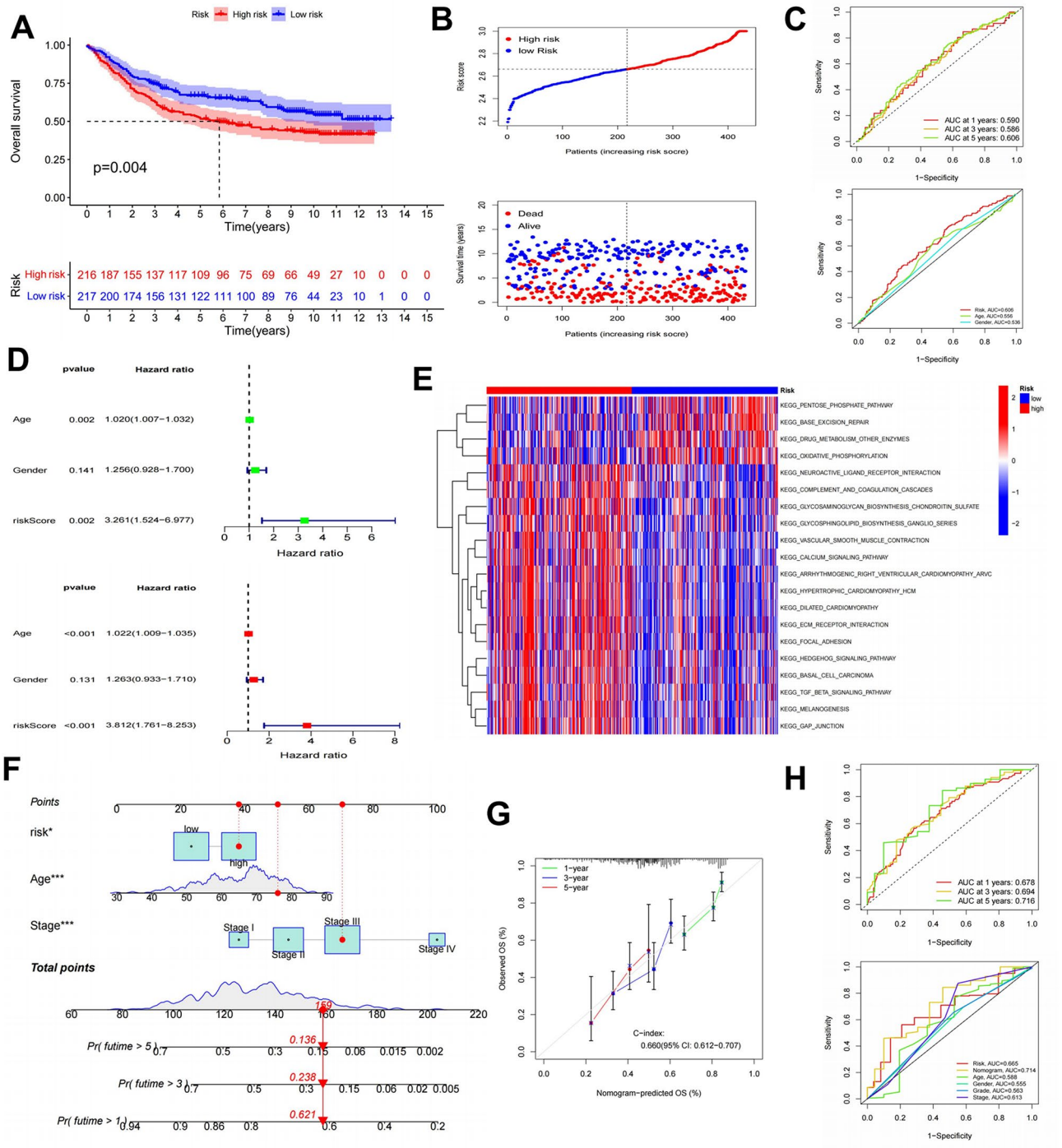

Fig. 5 Validation of the risk signature. (**A**) **K-M** analysis in the GSE84437 queue. **(B)** Distributions of risk scores and survival statuses in the GSE84437 cohort. **(C)** ROC curve for the risk signature and clinical characteristics in the GSE84437 cohort. **(D)** Univariate and multivariate Cox regression analyses in the GSE84437 cohort. **(E)** GSVA analysis for the risk signature. **(F)** A clinical nomogram constructed based on age, stage, and risk scores. **(G)** Calibration plot for the nomogram. **(H)** ROC curve for the nomogram and other clinical characteristics. K-M, Kaplan-Meier; ROC, receiver operating characteristics curve; GSVA, gene set variation analysis

Additionally, low-score patients had significantly longer OS in the age≤65, male, G3 level, T3-T4 stage, N1-N3 stage, and M0 subgroups (Figure S2 I-O).

Assessment of immune cell infiltration and immunological function

As seen in Fig. 6A, the stromal and immune scores of the high-risk group were significantly higher, indicating that the GC population with high-risk scores had a higher proportion of stromal cell and immune cell infiltration in the TME. After that, we explored the correlation between risk scores and immune function. Our analysis revealed that the low-risk group was primarily associated with functions like MHC class I and Th2 cells, whereas the high-risk group had higher levels of immune cell infiltration, including dendritic cells (DC), neutrophils, regulatory T cells (Treg), tumor-infiltrating lymphocytes (TIL), and so on (Fig. 6B). Likewise, we investigated the relationship between TIICs and risk scores using multiple methods. The findings demonstrated that, with the exception of activated CD4 T cells and type 17 T helper cells, which were negatively correlated with risk scores, the majority of tumor-infiltrating immune cells (TIICs), such as macrophage, myeloid-derived suppressor cells (MDSCs), and Treg, were positively correlated with risk scores. These cells demonstrated a higher proportion of infiltration in the high-risk group (Fig. 6C-F, Table S6).

Prediction of immunotherapy efficacy

The use of immunotherapy in cancer treatment has extremely high clinical value. However, its efficacy is limited to a subset of patients, as tumor cells can evade immune detection and develop resistance to immunotherapy [37]. The TIDE score can reflect the possibility of immune escape during immunotherapy and evaluate the potential clinical efficacy of immunotherapy in different risk groups. As shown in Fig. 6G, the TIDE, Dysfunction, and Exclusion scores of the high-risk scoring group were substantially higher than those of the low-risk scoring group. This suggests that patients in the high-risk scoring group are more likely to have immunological dysfunction and to develop resistance to immune therapy. We also studied the association between risk scores and several common immunological checkpoints (Fig. 7B). Additionally, we discovered a negative correlation between risk score and RNAss (Fig. 6H).

Microsatellites are repetitive sequences of small fragments of nucleic acids present in the genome with high mutagenicity. Functional defects in mismatch repair (MMR) proteins cause microsatellite instability (MSI), which raises the risk of tumor formation by inducing a high mutation phenotype in the genome. Microsatellites are classified into three groups based on their status: MSS, MSI-L, and MSI-H. The proportion of MSI-H varies significantly among tumor types, with a higher incidence observed in solid tumors such as GC, colorectal cancer (CRC), and endometrial cancer (EC) [38]. The detection of MSI is crucial for the diagnosis, treatment, and prognosis of various solid tumors, including CRC and EC. MSI-H is an independent prognostic marker for stage II colorectal cancer. Compared to MSS patients, those with MSI-H have a better prognosis for GC and small intestine adenocarcinoma [39, 40]. Likewise, MSI-H patients are more responsive to immunotherapy, benefiting from ICIs regardless of cancer type [41, 42]. Consequently, we analyzed the connection between risk scores and microsatellite status. Our findings revealed that the MSI-H group had the lowest risk score, and the low-risk group had a higher proportion of MSI-H (27% vs. 10%), indicating that the GC population with low-risk scores was more likely to benefit from immunotherapy (Fig. 7A, Table S7). Additionally, this study uncovered a relationship between risk scores and the effectiveness of ICIs. As Fig. 7C illustrated, patients in the low-risk group responded better to several ICI groups, including ctla4_neg_pd1_pos, ctla4_pos_pd1_neg, and ctla4_pos_pd1_pos.

We next investigated the somatic mutation data from the TCGA-STAD cohort and visualized the results using a waterfall plot. Researchers observed that the low-risk scoring group had a higher mutation frequency (93.68% vs. 88.04%), with missense mutation being the most common mutation and TTN being the gene with the greatest mutation frequency (Fig. 7D). In recent years, TMB has received great attention in studying ICI-related biomarkers. TMB can indirectly reflect the ability and degree of tumors to produce new antigens and has been proven to predict the efficacy of immunotherapy for various malignancies [43]. Treatment with ICIs is more likely to be beneficial for patients with high TMB (TMB-H). Therefore, we calculated the TMB value for each patient with GC and discovered that the low-risk group had a higher TMB score (Fig. 7E), and the TMB-H group had a longer OS time (Fig. 7F). Moreover, in the combined analysis of TMB and risk scores, the population with high TMB and low-risk scores had the longest OS and the best prognosis (Fig. 7G). Lastly, we also forecasted drug sensitivity based on the risk scores, finding that the low-risk score group exhibited lower IC50 values and higher sensitivity for a few commonly utilized chemotherapeutic agents, such as 5-Fluorouracil, Oxaliplatin, Irinotecan, and Cisplatin FigureS3A).

Determination CDH19 as a potential biomarker for GC

The researchers evaluated the diagnostic efficacy of genes in the signature model using ROC curves. The AUC for SLC7A2, CDH19, and CCN1 were 0.524, 0.793, and 0.487, respectively, with CDH19 showing the best diagnostic efficacy (Fig. 8A). Therefore, we

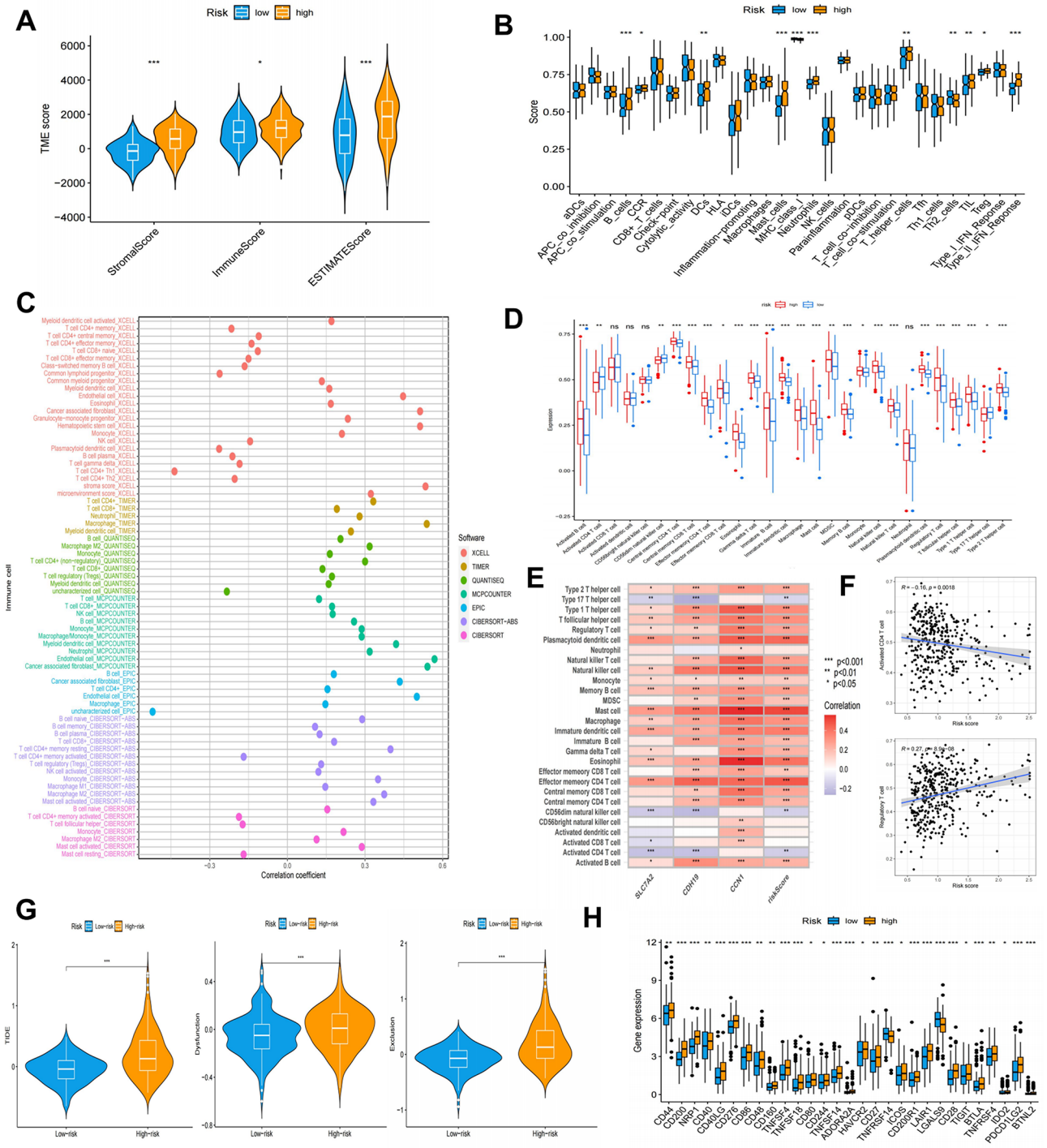

Fig. 6 The correlation between the risk signature and immune cell infiltration. (**A**) The stromal, immune, and estimate scores of GC patients. **(B)** Immune function analysis for risk subgroups. **(C-D)** Analyzing the infiltration levels of TIICs in high and low-risk groups using several algorithms. **(E)** Heatmap between the risk signature and immune infiltrating cells. **(F)** Spearman analysis between the risk signature and several TIICs, including activated CD4 T cell and regulatory T cell. **(G)** TIDE, dysfunction, and exclusion in high and low-risk groups. **(H)** Expression of ICIs in risk groups. $^{*}P < 0.05$; $^{**}P < 0.01$; $^{***}P < 0.001$. GC, gastric cancer; TIICs, tumor-infiltrating immune cells; TIDE, tumor immune dysfunction and exclusion; ICIs, immune checkpoint inhibitors

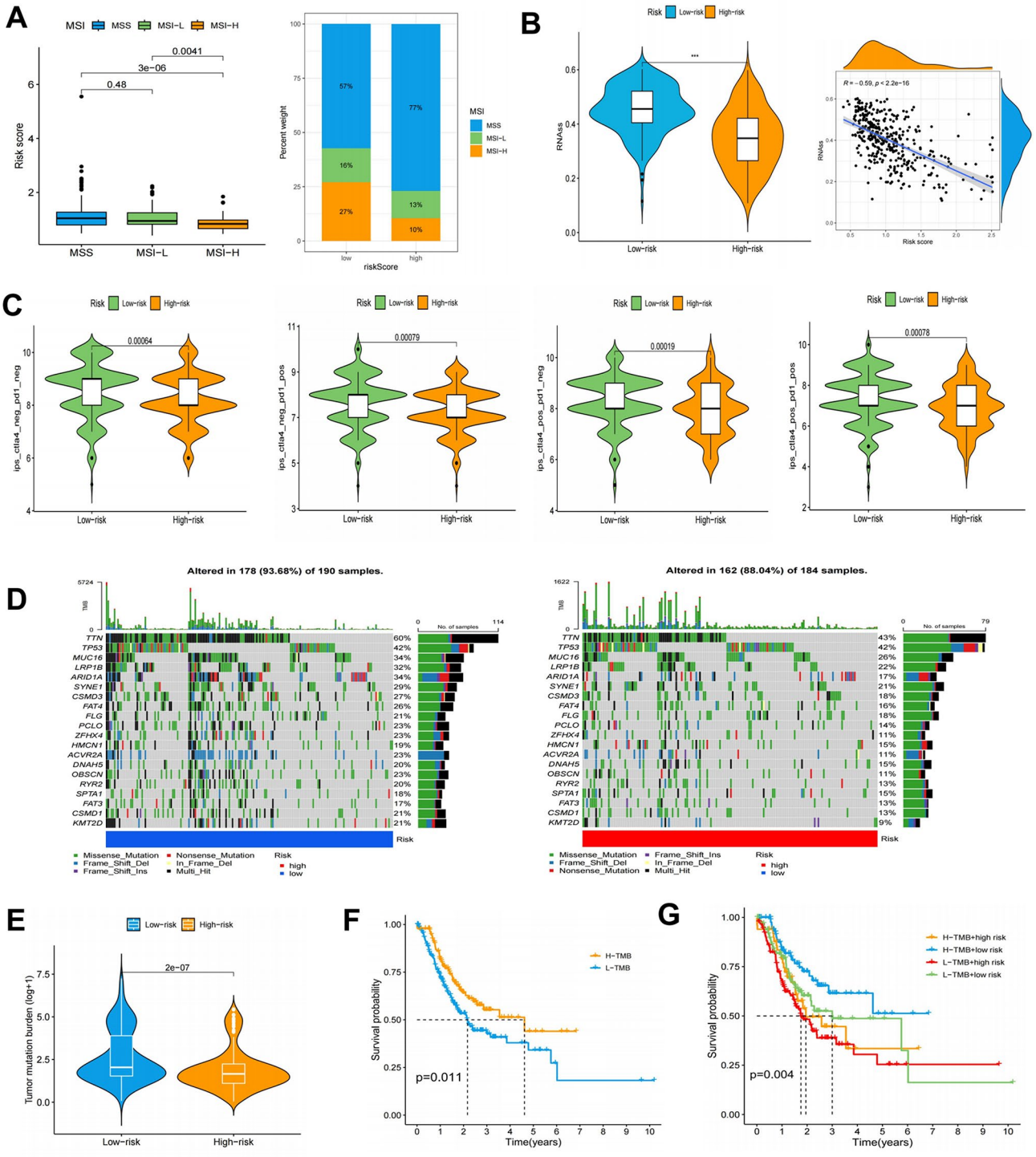

Fig. 7 Prediction of immunotherapy efficacy. (**A**) Analysis of risk scores and microsatellite state. **(B)** The correlation between risk scores and RNAss. **(C)** Predict the efficacy of anti-PD-1 and anti-CTLA-4 antibodies in the risk subgroup. **(D)** Waterfall diagram of somatic mutations in high and low risk scoring groups. **(E)** TMB scores in high and low-risk groups. **(F)** K-M curve of OS in high and low-TMB groups. **(G)** K-M curve survival curves among the four groups that combined TMB with risk signature. *$P < 0.05$; **$P < 0.01$; ***$P < 0.001$. RNAss, RNA stemness scores; TMB, tumor mutation burden; OS, overall survival. K-M, Kaplan-Meier; OS, overall survival

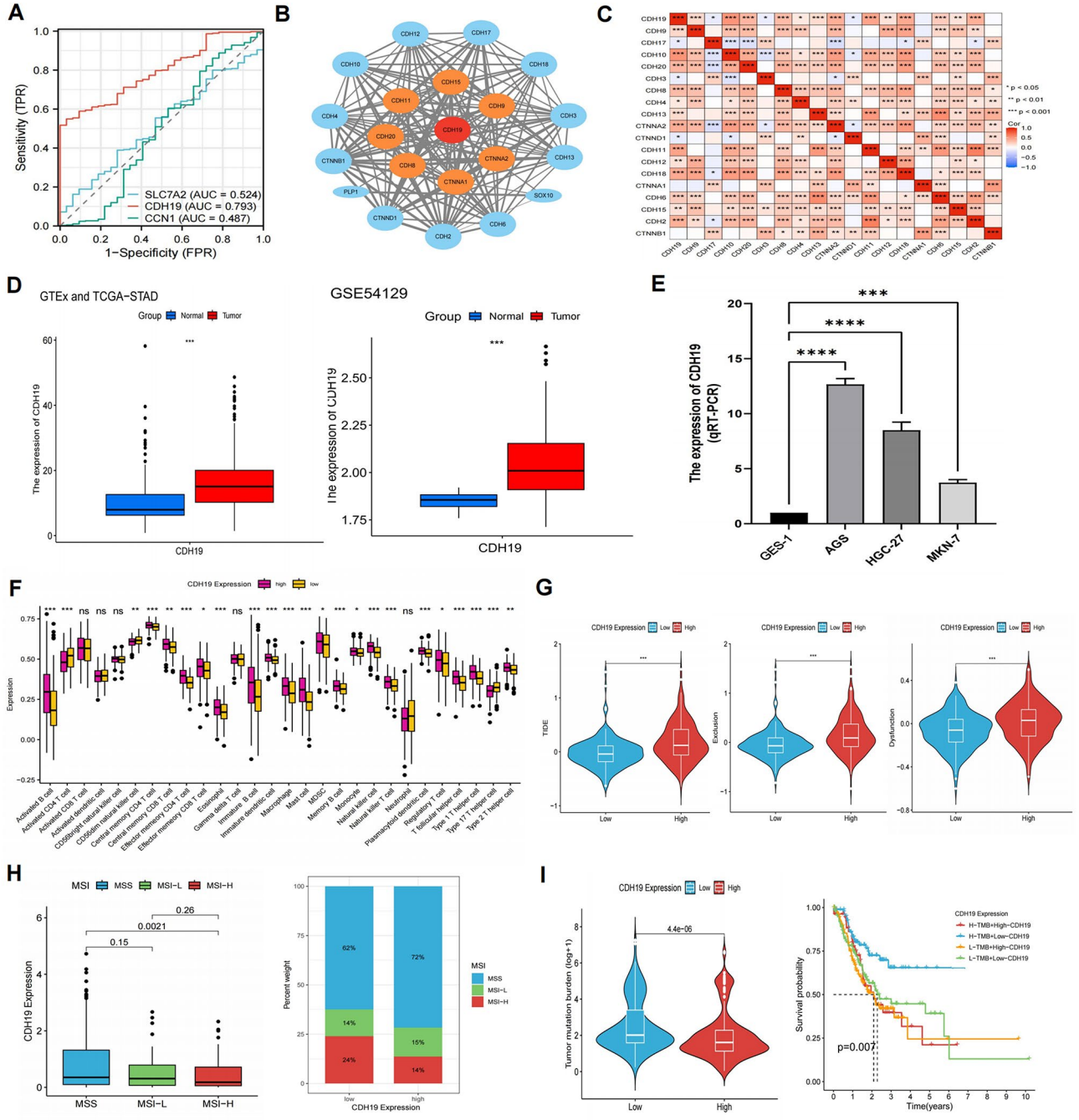

Fig. 8 Identifying CDH19 as a potential gastric cancer biomarker. (**A**) ROC curves for diagnosing gastric cancer, including SLC7A2, CDH19 and CCN1. **(B)** PPI network of proteins closely related to CDH19. **(C)** Heatmap of CDH19 and related genes. **(D)** The expression levels of CDH19 in GC tissue and normal gastric tissue, including GTEx database, TCGA-STAD cohort, and GSE54129 cohort. **(E)** Determination of CDH19 expression levels in gastric cancer cell lines and normal gastric epithelial cells by qRT -PCR, and the experiment was repeated three times. **(F)** Immune cell infiltration analysis of high and low CDH19 expression groups. **(G)** The tumor immune dysfunction and exclusion score of different CDH19 expression groups. **(H)** Evaluation of CDH19 expression and microsatellite status. **(I)** The relationship between CDH19 expression, TMB score, and prognosis. ns $P > 0.05$; *$P < 0.05$; **$P < 0.01$; ***$P < 0.001$. ROC, receiver operating characteristics curve; PPI, Protein-Protein Interaction; qRT-PCR, quantitative real-time polymerase chain reaction; GC gastric cancer; TCGA, The Cancer Genome Atlas; TMB, tumor mutation burden

decided to conduct further research on CDH19. Firstly, a PPI network of genes closely associated with CDH19 was constructed through the STRING website, and then imported into Cytoscape software for processing (Fig. 8B). The correlation heatmap showed that CDH19 had the highest correlation with CDH10, CDH11, and CDH18 (correlation coefficient > 0.4), with all p-values less than 0.001(Fig. 8C). To detect the expression of

CDH19 in GC and normal gastric tissues, the researchers included STAD samples from the GTEx database to reduce sample bias. After integration, a total of 620 samples were obtained, comprising 210 normal gastric samples and 410 GC samples. Visualization using the "limma" package revealed that CDH19 expression was higher in GC, suggesting that CDH19 may be play a role in the occurrence and development of GC. Subsequently, the researchers validated through the GSE54129 cohort that the expression level of CDH19 in GC was also higher than that in normal gastric tissue (Fig. 8D). Therefore, to verify CDH19 expression levels, we performed the qRT-PCR experiment and found that CDH19 was considerably up-regulated in GC cell lines (AGS, HGC-27, and MKN-7) (Fig. 8E). Additionally, we divided all individuals into high and low groups based on the expression of CDH19 and performed K-M analysis to better understand the impact of CDH19 on the prognosis of GC patients. The results revealed that OS, PFS, and DFS were shorter in the population with high CDH19 expression (Fig. 3H, S3B). As a result, we speculate that CDH19 may serve as a pro-oncogene and that patients with higher expression levels may have shorter lifetimes and worse prognoses. According to GSEA analysis, the high CDH19 expression population was associated with "PPAR_SIGNALING_PATHWAY", "MAPK_SIGNALING_PATHWAY", "HEDGEHOG_SIGNALING_PATHWAY", "FOCAL_ADHESION" and "GAP_JUNCTION"(Figure S3C), which were linked to the occurrence of cancer and matrix activation. Furthermore, ssGSEA analysis showed that the low CDH19 expression group had more activated CD4T cells infiltration, whereas the high CDH19 group had a higher proportion of immunosuppressive cells, such as macrophages, MDSCs, and Tregs (Fig. 8F). Similarly, for immunotherapy-related indicators and biomarkers, the CDH19 high expression group exhibited higher TIDE, Dysfusion, and Exclusion scores (Fig. 8G) but lower MSI-H ratios and TMB scores (Fig. 8H-I), illustrating that CDH19 can be used to direct clinical immunotherapy and forecast immune efficacy.

CDH19 affected the biological behavior of GC cells

We constructed RNAi negative control (sh-NC) and knockdown CDH19 (sh-CDH19) lentiviral vectors to evaluate the role of CDH19 in promoting GC cell proliferation, invasion, and metastasis. After transfecting them into the AGS and HGC-27 cell lines, we validated the knockdown effect using qRT-PCR assay. Figure 9A and B demonstrated that sh-CDH19-1 and sh-CDH19-2 in AGS, as well as sh-CDH19-2 and sh-CDH19-3 in HGC-27, exhibited the most pronounced knockdown effects. Thus, we selected the cells above for subsequent phenotypic experiments. Cell viability and proliferation were assessed using the MTT assay and colony formation assay. The findings indicated that the AGS knockdown group (Fig. 9C, E, H) and the HGC-27 knockdown group (Fig. 9D, F, H) had considerably lower cell viability and proliferation capacity than the control group (sh-NC). Following this, a 48-hour wound-healing experiment revealed that the migration ability of GC cells in the sh-CDH19 group was significantly reduced (Fig. 9G). All experimental data in Table S8. Thus, we preliminarily infer that knocking down CDH19 expression inhibited the growth and migration of GC.

CDH19 affects ferroptosis and oxidative stress in GC cells

As shown in Fig. 9I, researchers used FerroOrange reagent for iron staining and found that the intensity and concentration of iron ion staining were higher in sh-CDH19 cells. The expression level of ACSL4 is lower in GES-1 cells, while the expression level of GPX4 is higher in AGS and HGC-27 cells (Fig. 10A), ACSL4, a lipid metabolism enzyme, is known to promote ferroptosis when its expression or activity is elevated [44], indicating that ferroptosis may be involved in the occurrence of GC. Subsequently, Western blot results exhibited an increase in ACSL4 transcription levels in the sh-CDH19 group, and a decrease in GPX4 transcription levels (Fig. 10B). Therefore, CDH19 may be involved in regulating ACSL4 and GPX4 related pathways, thereby affecting the occurrence of ferroptosis.In addition, to explore whether CDH19 influences the oxidative stress process, we used DCFH-DA and DHE reagents to measure ROS levels in GC cells. The study discovered that ROS was significantly increased in the sh-CDH19 groups of AGS and HGC-27 cell line (Fig. 10C, D), implying that suppressing CDH19 expression may enhance oxidative stress and increase ROS accumulation.

Discussion

GC is a malignant tumor with a high incidence rate and mortality, and its overall prognosis is unfavorable. In recent years, immunotherapy, mainly with ICIs, has significantly improved the objective response rate (ORR) and OS of patients with advanced malignant tumors. Nevertheless, the overall treatment effectiveness rate is less than 20%, and the cost is generally expensive, often accompanied by varying degrees of immune-related adverse reactions. Therefore, it is urgent to find accurate and reliable biomarkers to screen potential beneficiaries of immunotherapy.

The underlying mechanism of ferroptosis, an iron-dependent cell death, is lipid peroxidation induced by oxidative stress. The primary cause of ferroptosis is the build-up of ROS, which leads to lipid peroxidation and exceeds the redox levels of glutathione (GSH) and GPX4. This disrupts cell membrane integrity and ultimately triggers cell death [45]. Iron, lipids, and ROS play

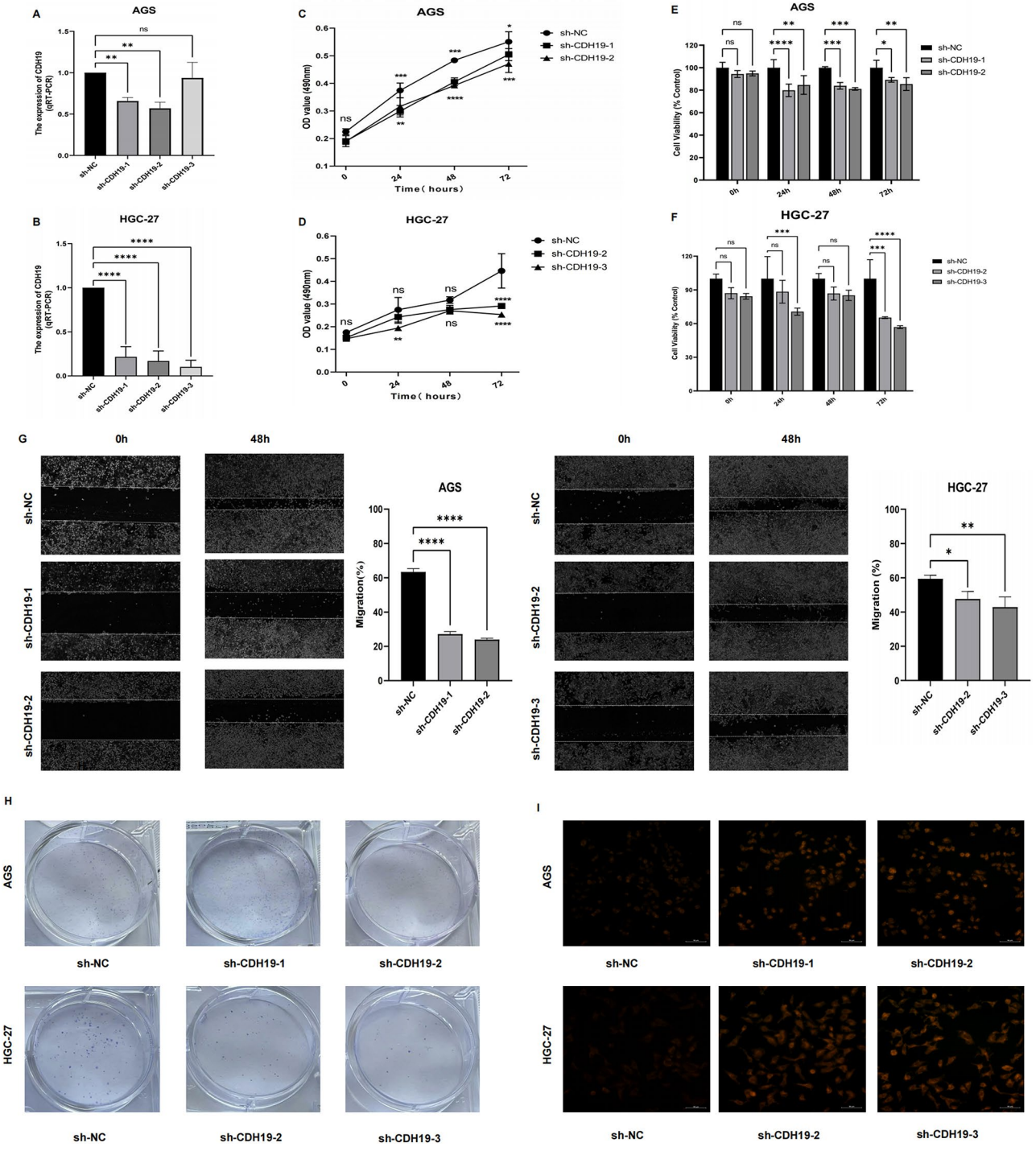

Fig. 9 CDH19 promotes the proliferation and migration of GC cells. (**A, B**) The expression of CDH19 in gastric cancer cell control (sh-NC) and knockdown (sh-CDH19) groups was examined utilized the qRT-PCR assay and select the two cell lines with the most obvious knockdown for subsequent experiments, repeating the experiment three times. **(C-F)** The MTT assay was employed to evaluate the proliferation and viability of AGS and HGC-27 GC cells. **(G)** The wound-healing experiment assessed the GC cell' migration capacity and calculate its migration rate. **(H)** Colony formation experiments of AGS and HGC-27 cells lines, including sh-NC and sh-CDH19 groups. **(I)** Iron staining of AGS and HGC-27 cells lines. ns $P > 0.05$; *$P < 0.05$; **$P < 0.01$; ***$P < 0.001$. **** $P < 0.0001$. GC, gastric cancer; qRT-PCR, quantitative real-time polymerase chain reaction

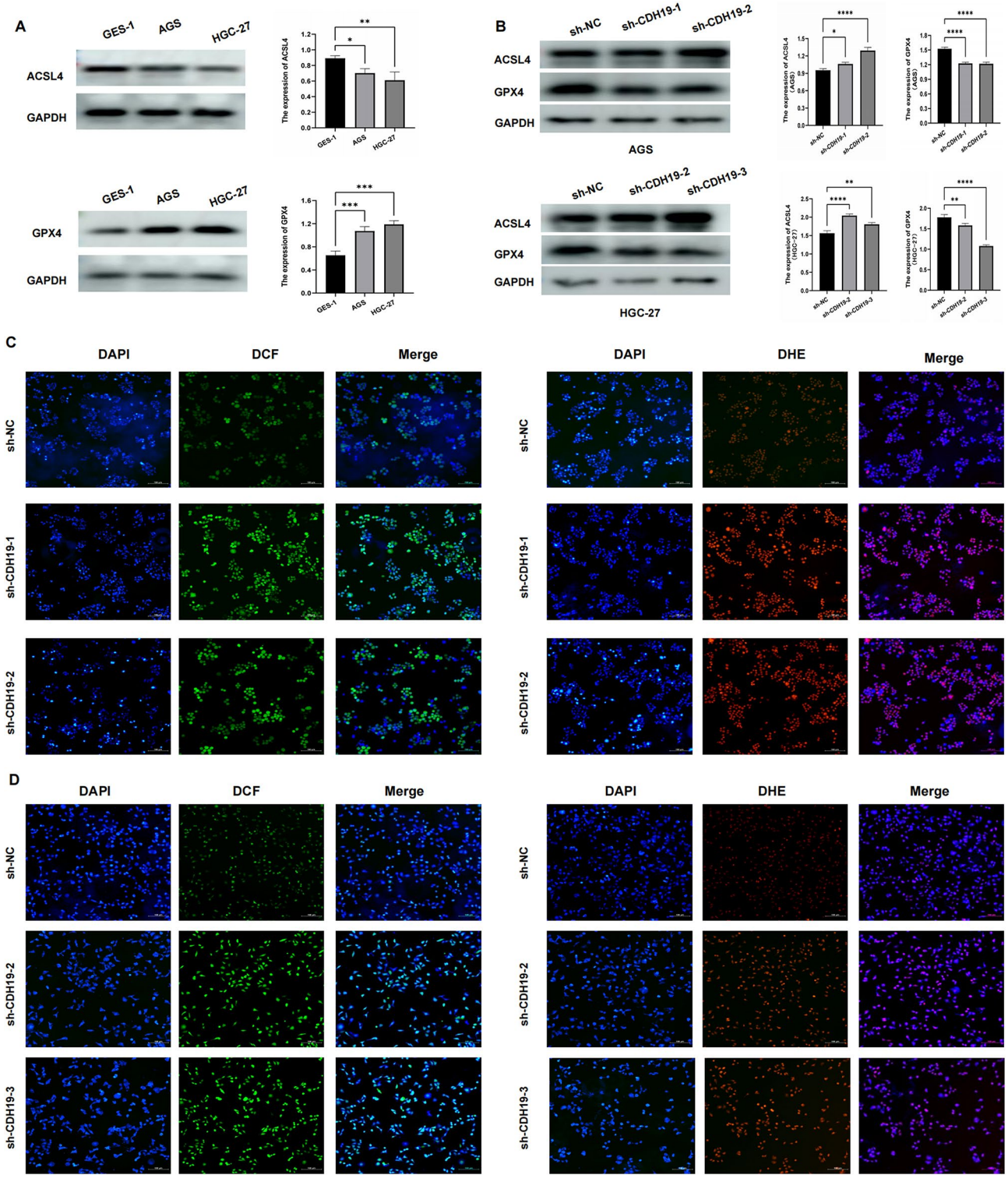

Fig. 10 CDH19 participates in ferroptosis and oxidative stress. **(A)** Expression levels of ACSL4 and GPX4 in GES-1, AGS and HGC-27 cell lines. **(B)** Exploring the effect of CDH19 on ferroptosis-related proteins GPX4 and ACSL4 in GC cells through Western-blot experiments. **(C-D)** Exploring the effect of CDH19 on reactive oxygen species levels in GC cells through immunofluorescence staining. Above experiments were repeated three times. GC, gastric cancer; GPX4, glutathione peroxidase 4

irreplaceable roles in the process of ferroptosis. Ferroptosis is regulated by multiple cellular metabolic pathways, including mitochondrial activity, sugar, amino acid, and lipid metabolism, as well as signaling pathways related to cell proliferation and tumor progression [46]. Tumor cells can evade ferroptosis and promote cancer metastasis by limiting the synthesis and peroxidation of PUFA-PL, restricting the supply of unstable iron, and upregulating the cellular defense system [6]. According to reports, the inactivation of tumor suppressor factors such as p53, BAP1, and KEAP1, or the activation of the oncogene KRAS, can upregulate the expression of SLC7A11, leading to a reduction in ferroptosis in tumor cells [18, 47]. Tumor cells also avoid ferroptosis through metabolic reprogramming. For example, when insufficient energy metabolism causes a decrease in ATP content, cancer cells activate the AMPK signaling pathway, thereby reducing PUFA synthesis and ultimately decreasing ferroptosis. Therefore, inhibiting the AMPK-ACC-PUFA signaling pathway may produce anti-tumor effects and enhance the efficacy of immunotherapy and chemotherapy treatment [48].

Additionally, PI3K-AKT mTOR is one of the most frequently mutated signaling pathways in cancer, with both mTORC1 and mTORC2 involved in ferroptosis. mTORC2 can phosphorylate SLC7A11 and inhibit its transport activity. Activating the LATS1/2 kinase in the Hippo pathway can lead to the inactivation of mTORC1, preventing the degradation of SLC7A11 in lysosomes. Moreover, the PI3K-AKT mTORC1 signaling pathway plays a crucial role in maintaining cellular redox balance through NRF2-mediated signal transduction and SREBP1/SCD1-mediated MUFA synthesis [49]. Literature has demonstrated that ferroptosis can induce GC cell death, and its combination with various chemotherapy drugs is expected to overcome drug resistance in GC patients [50]. Given the poor prognosis of GC, it is crucial to identify genes related to oxidative stress and ferroptosis as clinical diagnostic and therapeutic markers for GC.

This study successfully developed a prognostic signature for OFRGs through bioinformatics analysis and experiments. Besides, CDH19 was identified and validated as a potential biomarker for GC. We initially employed expression and mutation analysis on OFRGs and investigated their relationship with the prognosis of GC. Afterwards, consensus clustering analysis divided all GC samples into two clusters (K=2). The Kaplan-Meier survival analysis revealed that cluster A had a more extended OS period, and immune infiltration analysis indicated that cluster B had a higher level of immune cell infiltration. Enrichment analysis showed that cluster B was closely related to signaling pathways such as "IL-17", "PI3K Akt", and "JAK-STAT." Subsequently, a prognostic signature for OFRGs, including SLC7A2, CDH19, and CCN1, was constructed via LASSO and multivariate Cox analysis. In the TCGA-STAD and GSE84437 queues, the survival of high-risk score populations was substantially shorter, and mortality risk was significantly increased. The risk scores of cluster B and gene cluster A were elevated, confirming the consistency of the above analysis. The ROC curve suggested that the predictive ability of the risk signature is superior to conventional clinical pathological parameters. Further, univariate, and multivariate Cox analysis indicated that age, stage, and risk score are all risk factors for the prognosis of GC. Following that, we employed GSVA to perform functional analysis on the high and low-risk groups, discovering that the low-risk group's enriched pathways were primarily related to cellular metabolism and function. In contrast, the high-risk group was linked to signaling pathways associated with cell proliferation and cancer development, such as "TGF-β," "Hedgehog," "MTOR," and "MAPK." Next, we established a clinical nomogram based on age, stage, and risk score, and the nomogram prediction's reliability was validated using the calibration and ROC curves.

TME is a dynamic ecosystem composed of cellular components such as tumor cells, immune cells, stromal cells, and non-cellular components such as extracellular matrix and blood vessels. These elements interact with each other and affect the growth and progression of tumors [51]. The relationship between ferroptosis and TME is complicated. On the one hand, ferroptosis in cancer cells can trigger or regulate immune responses in TME. On the other hand, immune cells in TME exhibit significant differences in sensitivity to ferroptosis, and different types of immune cells can enhance or inhibit ferroptosis in cancer cells [52]. Due to the intricate TME and insufficient immune system activation, tumor cells undergo immune escape, resulting in limited immune therapy response in many cancer patients. ICIs based on tumor cell ferroptosis are expected to provide new strategies for improving ferroptosis-mediated immunotherapy. In the analysis of immune function and immune infiltration, researchers discovered that the infiltrating proportion of stromal cells and immune cells (especially neutrophils, M2 macrophages, MDSC, T-regs) in the TME was higher in populations with high-risk scores. These cells can shape an immune-suppressive microenvironment within tumors, trigger immunological escape, and develop immune resistance, thereby promoting cancer occurrence and progression [53, 54]. Considering the high clinical value of ICIs in treating cancer, researchers are exploring the role of risk scores in predicting the effectiveness of immunotherapy. In the high-risk population, TIDE, Dysfunction, and Exclusion scores are significantly higher, indicating a higher probability of immune dysfunction and resistance to immunotherapy resistance

in these patients. In addition, we analyzed the relationship between risk scores and microsatellite status. The MSI-H group exhibited the lowest risk score, and the low-risk group had a higher proportion of MSI-H and increased response rates to different ICI treatments. Subsequently, through somatic mutation analysis, we found that the low-risk scoring group had higher mutation frequency, elevated TMB score, and more prolonged OS, indicating a greater likelihood of benefiting from immunotherapy in the GC population with low-risk scores.

Following that, the researchers discovered the differential expression of CDH19 between GC and para-cancer tissues, and the qRT-PCR experiment demonstrated that CDH19 was significantly upregulated in GC cell lines. CDH19 is one of the type II cadherin genes located in chromosome cluster 18 and is an important member of the cadherin family. This family consists of 23 members, among which the widely studied cadherin proteins include epithelial (E -) cadherin (CDH1), neural (N -) cadherin (CDH2), placental (P -) cadherin (CDH3), and retinal (R -) cadherin (CDH4). The cadherin family, comprising transmembrane glycoproteins, mediates calcium dependent intercellular adhesion and regulates cell growth and differentiation [55]. The changes in the expression of cadherins play a crucial role in tumorigenesis, tumor progression, angiogenesis, and tumor immune response [56]. For example, dysregulation of the cadherin catenin complex can activate oncogenic pathways, including Wnt and TGF - β, which contribute to epithelial mesenchymal transition (EMT) and promote cancer occurrence and metastasis [57]. The characteristic of EMT is the loss of CDH1 expression and the accompanying upregulation of CDH2, which is associated with increased migration and invasiveness as well as poor prognosis. In addition, epigenetic reprogramming of EMT promotes ferroptosis in cancer cells. The EMT markers CDH1 and ZEB1 are closely related to the ferroptosis sensitivity of cancer cells. Previous studies have reported that CDH1 mediated cell-cell contact inhibits ferroptosis by activating the intracellular NF2-YAP1 and Hippo signaling pathways, indicating that the maintenance of NF2 and CDH1 inhibits ferroptosis related lipid peroxidation and cell death [16]. In diffuse GC, functional loss mutations in CDH1 have also been shown to increase sensitivity to ferroptosis [58]. HPCAL1-dependent CDH2 depletion increases susceptibility to ferroptosis by reducing membrane tension and promoting lipid peroxidation. Conversely, CDH2-mediated increase in membrane tension inhibits ferroptosis, potentially due to effects on membrane fluidity and the uptake of iron and other extracellular metabolites [59]. It is reported that the overexpression of CDH1/2/4/11/12/13 mRNA in breast cancer is associated with extracellular matrix remodeling, EMT activation and WNT/β - catenin signaling pathway imbalance, leading to poor prognosis in breast cancer patients [55]. In addition, studies have shown that overexpression of CDH4 in oral squamous cell carcinoma (OSCC) can promote the proliferation, invasion, and migration of cancer cells, which may be related to the EMT pathway. Researchers have confirmed through experiments that in OSCC the downregulation of CDH4 leads to a decrease in GPX4 and GSH, a decrease in GSH/GSSG ratio, and an increase in GSSG and MDA, revealing that CDH4 can resist cell sensitivity to ferroptosis and reduce cell death by inhibiting ferroptosis [60]. CDH19 is related to the prognosis of numerous types of cancer. The OS period of patients with high expression of CDH19 in cervical cancer is significantly longer [61], but those with high CDH19 expression in bladder cancer have a dismal prognosis [62]. According to reports, CDH19 inhibits cervical cancer cell proliferation as well as the activation of the AKT and NF- κB signaling pathways, which may be a potential therapeutic target for cervical cancer [61]. In addition, in triple-negative breast cancer (TNBC), the hsa_circ_0006220/miR-197-5p/CDH19 pathway may contribute to disease progression [63]. In summary, these studies suggest that cadherins (CDHs) may be potential targets for cancer treatment. The CDH family is closely associated with ferroptosis and may act as a biomarker for predicting cancer cell susceptibility to ferroptosis. Nevertheless, the relationship between CDH19 and the pathogenesis and prognosis of GC is still unclear, and the relationship between CDH19 and ferroptosis has not been fully explored.

Researchers performed K-M analysis in CDH19 differentially expressed population, discovering that the population with high CDH19 expression had a worse prognosis. Therefore, we speculate that CDH19 may be a risk factor for GC. Through GSEA analysis, researchers revealed that the high CDH19 expression is correlated to cancer activation related signaling pathways such as PPAR, MAPK, Hedgehog, as well as intercellular adhesion pathways such as FOCAL-ADHESION and GAP_JUNCTION. Moreover, populations with high CDH19 expression exhibit lower infiltration of activated CD4 T cells with anti-tumor effects, but a higher percentage of immunosuppressive cells, such as M2 macrophages and Tregs. The high and low CDH19 groups differ significantly in the expression of markers linked to immunotherapy, suggesting that CDH19 can also be utilized to direct clinical immunotherapy and forecast immune efficacy.

Later, researchers constructed GC cell lines with knockdown CDH19 expression and validated the effect. The MTT cell viability analysis and colony formation assays displayed that compared with the control group (sh-NC), the AGS and HGC-27 knockdown groups (sh-CDH19) exhibited a significant decrease in GC cell

viability and proliferation. Furthermore, the wound healing experiment demonstrated a marked reduction in the migratory ability of GC cell in the CDH19 knockdown group. Consequently, we preliminarily confirmed that CDH19 promoted GC cell migration and proliferation. Additionally, we observed significantly higher levels of ROS in the CDH19 knockdown group of AGS and HGC-27 cell lines. Further, Western blot findings revealed that the transcription level of GPX4 in the sh-CDH19 group decreased while the expression level of ACSL4 increased. GPX4 is a crucial resistance factor to ferroptosis, maintaining intracellular redox balance by inhibiting lipid peroxidation and catalytic reduction reactions [64]. Currently, the XC-/GSH/GPX4 system is one of the extensively studied pathways for ferroptosis inhibition. Cystine enters cells through the XC- system and generates cysteine under the action of GSH, participating in GPX4 clearing lipid peroxides. SLC7A11 is a transporter subunit of the XC- system, and blocking SLC7A11-mediated cysteine transport can induce ferroptosis in various cancer cells [6, 65]. Additionally, under stress, the activation of Nrf2 directly or indirectly promotes the expression of GPX4 [66], and HSPA5 also upregulates the expression of GPX4 by inhibiting p53 [67]. The activated XC- system enriches intracellular cysteine, thereby regulating the mTORC1/4EBP1/GPX4 pathway to promote GPX4 synthesis, reduce GPX4 degradation, and resist ferroptosis [68]. Overall, GPX4 plays a dual role in cancers. On the one hand, reducing GPX4 levels induces ferroptosis in cancer cells, thereby inhibiting cancer proliferation, development, and recurrence. On the other hand, GPX4 reshapes TME and regulates the cancer process by promoting angiogenesis and immune response [69]. In summary, high levels of GPX4 are often seen as markers of poor prognosis. Furthermore, ACSL4 is a lipid metabolism enzyme that enhances the generation of lipid peroxides. ACSL4 promotes ferroptosis by promoting the esterification of PUFAs to acyl CoA (acyl CoA). It is worth noting that in a cell subgroup of triple-negative breast cancer, the expression level of ACSL4 is related to their sensitivity to ferroptosis inducers, and a similar correlation is observed in drug-resistant mesenchymal carcinoma cells and clear cell renal carcinoma cells. Therefore, ACSL4 is an important pharmacological target for treating ferroptosis-related diseases. Therefore, we conjectured that CDH19 is involved in regulating ACSL4 and GPX4-related pathways. Knocking down CDH19 leads to decreased GPX4 transcription and increased ACSL4 transcription, leading to reduced intracellular reduction capacity, accumulation of ROS, and promotion of ferroptosis, ultimately causing GC cell death.

It is necessary to recognize the limitations of this work. Firstly, although the researchers combined normal gastric tissue samples from the TCGA-STAD and GTEx databases to reduce bias and used GSE54129 as an independent cohort to validate the differential expression of CDH19, the total sample size is still insufficient. A larger cohort of GC patients, particularly from Asia, needs to be included. Secondly, in the TCGA-STAD and GSE84437 cohorts, GC patients with high expression of CDH19 had a worse prognosis, suggesting that CDH19 is a risk factor for GC, but further clinical validation is needed. In addition, this study preliminarily demonstrated that CDH19 can promote the proliferation and migration of GC cells and explored the involvement of CDH19 in ferroptosis and oxidative stress. However, the exact mechanism has not been fully elucidated, and a large amount of data and experiments are still needed to explore how CDH19 affects GC proliferation and ferroptosis. In addition, the complex interaction between ferroptosis and TME may affect the progression of GC, a field that has not been fully explored, and warrants further investigation in the future.

Conclusions

This article revealed that the OFRGs signature model can predict the prognosis of GC. We also identified CDH19 as a potential biomarker for GC and preliminarily demonstrated its involvement in the processes of ferroptosis and oxidative stress.

Supplementary Information

The online version contains supplementary material available at https://doi.org/10.1186/s40246-024-00682-w.

Supplementary Material 1
Supplementary Material 2
Supplementary Material 3
Supplementary Material 4
Supplementary Material 5
Supplementary Material 6
Supplementary Material 7
Supplementary Material 8
Supplementary Material 9
Supplementary Material 10
Supplementary Material 11

Acknowledgements

We thank the researchers and participants in the public database that was utilized for this study, as well as the editor and reviewers for their valuable comments.

Author contributions

All authors have made contributions to the article. This study was conceived by SW, WQ, and JG. The data was gathered and evaluated by SW and XL. RW and MZ visualize data. SZ and XL conducted experimental verification. The article is written by SZ, RW, CL and SW. The manuscript is thoroughly reviewed and revised by WQ and SW. All authors examined and approved the final submission.

Funding
The study was supported by Qingdao Key Clinical Specialty Elite Discipline and Beijing Xisike Clinical Oncology Research Foundation (Grant No.Y-HR2018-185, Grant No.Y2019-AZZD-0471).

Data availability
No datasets were generated or analysed during the current study.

Declarations

Ethical approval
No ethical approval is required for this study.

Consent for publication
All authors agree to publish.

Competing interests
The authors declare no competing interests.

Author details
[1]Department of Oncology, The Affiliated Hospital of Qingdao University, Qingdao, Shandong Province 266000, China

Received: 14 August 2024 / Accepted: 9 October 2024
Published online: 05 November 2024

References

1. Siegel RL, Giaquinto AN, Jemal A. Cancer statistics, 2024. CA Cancer J Clin. 2024;74(1):12–49. https://doi.org/10.3322/caac.21820.
2. López MJ, Carbajal J, Alfaro AL, Saravia LG, Zanabria D, Araujo JM, et al. Characteristics of gastric cancer around the world. Crit Rev Oncol Hematol. 2023;181:103841. https://doi.org/10.1016/j.critrevonc.2022.103841.
3. Karimi P, Islami F, Anandasabapathy S, Freedman ND, Kamangar F. Gastric cancer: descriptive epidemiology, risk factors, screening, and prevention. Cancer Epidemiol Biomarkers Prev. 2014;23(5):700–13. https://doi.org/10.1158/1055-9965.Epi-13-1057.
4. Smyth EC, Nilsson M, Grabsch HI, van Grieken NC, Lordick F. Gastric cancer. *Lancet*. (2020);396(10251):635–48. https://doi.org/10.1016/s0140-6736(20)31288-5
5. Guan WL, He Y, Xu RH. Gastric cancer treatment: recent progress and future perspectives. J Hematol Oncol. 2023;16(1):57. https://doi.org/10.1186/s13045-023-01451-3.
6. Jiang X, Stockwell BR, Conrad M. Ferroptosis: mechanisms, biology and role in disease. Nat Rev Mol Cell Biol. 2021;22(4):266–82. https://doi.org/10.1038/s41580-020-00324-8.
7. Tang D, Chen X, Kang R, Kroemer G. Ferroptosis: molecular mechanisms and health implications. Cell Res. 2021;31(2):107–25. https://doi.org/10.1038/s41422-020-00441-1.
8. Conrad M, Pratt DA. The chemical basis of ferroptosis. Nat Chem Biol. 2019;15(12):1137–47. https://doi.org/10.1038/s41589-019-0408-1.
9. Zhang DL, Ghosh MC, Rouault TA. The physiological functions of iron regulatory proteins in iron homeostasis - an update. Front Pharmacol. 2014;5:124. https://doi.org/10.3389/fphar.2014.00124.
10. Kuhn H, Banthiya S, van Leyen K. Mammalian lipoxygenases and their biological relevance. Biochim Biophys Acta. 2015;1851(4):308–30. https://doi.org/10.1016/j.bbalip.2014.10.002.
11. Zou Y, Li H, Graham ET, Deik AA, Eaton JK, Wang W, et al. Cytochrome P450 oxidoreductase contributes to phospholipid peroxidation in ferroptosis. Nat Chem Biol. 2020;16(3):302–9. https://doi.org/10.1038/s41589-020-0472-6.
12. Hao X, Zheng Z, Liu H, Zhang Y, Kang J, Kong X et al. Inhibition of APOC1 promotes the transformation of M2 into M1 macrophages via the ferroptosis pathway and enhances anti-PD1 immunotherapy in hepatocellular carcinoma based on single-cell RNA sequencing. *Redox Biol*. (2022);56:102463. https://doi.org/10.1016/j.redox.2022.102463
13. Yang F, Xiao Y, Ding JH, Jin X, Ma D, Li DQ, et al. Ferroptosis heterogeneity in triple-negative breast cancer reveals an innovative immunotherapy combination strategy. Cell Metab. 2023;35(1):84–e1008. https://doi.org/10.1016/j.cmet.2022.09.021.
14. Zou J, Wang L, Tang H, Liu X, Peng F, Peng C. Ferroptosis in Non-small Cell Lung Cancer: progression and therapeutic potential on it. Int J Mol Sci. 2021;22(24). https://doi.org/10.3390/ijms222413335.
15. Lee H, Zandkarimi F, Zhang Y, Meena JK, Kim J, Zhuang L, et al. Energy-stress-mediated AMPK activation inhibits ferroptosis. Nat Cell Biol. 2020;22(2):225–34. https://doi.org/10.1038/s41556-020-0461-8.
16. Wu J, Minikes AM, Gao M, Bian H, Li Y, Stockwell BR et al. Intercellular interaction dictates cancer cell ferroptosis via NF2-YAP signalling. *Nature*. (2019);572(7769):402–6. https://doi.org/10.1038/s41586-019-1426-6
17. Yang WH, Ding CC, Sun T, Rupprecht G, Lin CC, Hsu D, et al. The Hippo Pathway Effector TAZ regulates ferroptosis in renal cell carcinoma. Cell Rep. 2019;28(10):2501–e84. https://doi.org/10.1016/j.celrep.2019.07.107.
18. Forman HJ, Zhang H. Targeting oxidative stress in disease: promise and limitations of antioxidant therapy. Nat Rev Drug Discov. 2021;20(9):689–709. https://doi.org/10.1038/s41573-021-00233-1.
19. Hayes JD, Dinkova-Kostova AT, Tew KD. Oxidative stress in Cancer. *Cancer Cell*. (2020);38(2):167–97. https://doi.org/10.1016/j.ccell.2020.06.001
20. Farahzadi R, Valipour B, Fathi E, Pirmoradi S, Molavi O, Montazersaheb S, et al. Oxidative stress regulation and related metabolic pathways in epithelial-mesenchymal transition of breast cancer stem cells. Stem Cell Res Ther. 2023;14(1):342. https://doi.org/10.1186/s13287-023-03571-6.
21. Franchini F, Palatucci G, Colao A, Ungaro P, Macchia PE, Nettore IC. Obesity and thyroid Cancer risk: an update. Int J Environ Res Public Health. 2022;19(3). https://doi.org/10.3390/ijerph19031116.
22. Yu Y, Wu Y, Zhang Y, Lu M, Su X. Oxidative stress in the tumor microenvironment in gastric cancer and its potential role in immunotherapy. FEBS Open Bio. 2023;13(7):1238–52. https://doi.org/10.1002/2211-5463.13630.
23. Gorrini C, Harris IS, Mak TW. Modulation of oxidative stress as an anticancer strategy. Nat Rev Drug Discov. 2013;12(12):931–47. https://doi.org/10.1038/nrd4002.
24. The Gene Ontology Resource. 20 years and still GOing strong. Nucleic Acids Res. 2019;47(D1):D330–8. https://doi.org/10.1093/nar/gky1055.
25. Kanehisa M, Goto S. KEGG: kyoto encyclopedia of genes and genomes. Nucleic Acids Res. 2000;28(1):27–30. https://doi.org/10.1093/nar/28.1.27.
26. Zhang H, Meltzer P, Davis S. RCircos: an R package for Circos 2D track plots. BMC Bioinformatics. 2013;14:244. https://doi.org/10.1186/1471-2105-14-244.
27. Ritchie ME, Phipson B, Wu D, Hu Y, Law CW, Shi W, et al. Limma powers differential expression analyses for RNA-sequencing and microarray studies. Nucleic Acids Res. 2015;43(7):e47. https://doi.org/10.1093/nar/gkv007.
28. Wilkerson MD, Hayes DN. ConsensusClusterPlus: a class discovery tool with confidence assessments and item tracking. Bioinformatics. 2010;26(12):1572–3. https://doi.org/10.1093/bioinformatics/btq170.
29. Hänzelmann S, Castelo R, Guinney J. GSVA: gene set variation analysis for microarray and RNA-seq data. BMC Bioinformatics. 2013;14:7. https://doi.org/10.1186/1471-2105-14-7.
30. Daniel D, West-Mitchell K. The Sankey diagram: an exploratory application of a data visualization tool. *Transfusion*. (2024). https://doi.org/10.1111/trf.17803
31. Balachandran VP, Gonen M, Smith JJ, DeMatteo RP. Nomograms in oncology: more than meets the eye. Lancet Oncol. 2015;16(4):e173–80. https://doi.org/10.1016/s1470-2045(14)71116-7.
32. Obuchowski NA, Bullen JA. Receiver operating characteristic (ROC) curves: review of methods with applications in diagnostic medicine. Phys Med Biol. 2018;63(7):07tr1. https://doi.org/10.1088/1361-6560/aab4b1.
33. Yoshihara K, Shahmoradgoli M, Martínez E, Vegesna R, Kim H, Torres-Garcia W, et al. Inferring tumour purity and stromal and immune cell admixture from expression data. Nat Commun. 2013;4:2612. https://doi.org/10.1038/ncomms3612.
34. Zhao F, Zhao C, Xu T, Lan Y, Lin H, Wu X, et al. Single-cell and bulk RNA sequencing analysis of B cell marker genes in TNBC TME landscape and immunotherapy. Front Immunol. 2023;14:1245514. https://doi.org/10.3389/fimmu.2023.1245514.
35. Liu TT, Li R, Huo C, Li JP, Yao J, Ji XL, et al. Identification of CDK2-Related Immune Forecast Model and ceRNA in Lung Adenocarcinoma, a Pan-cancer Analysis. Front Cell Dev Biol. 2021;9:682002. https://doi.org/10.3389/fcell.2021.682002.
36. Maeser D, Gruener RF, Huang RS. oncoPredict: an R package for predicting in vivo or cancer patient drug response and biomarkers from cell line screening data. Brief Bioinform. 2021;22(6). https://doi.org/10.1093/bib/bbab260.
37. Riley RS, June CH, Langer R, Mitchell MJ. Delivery technologies for cancer immunotherapy. Nat Rev Drug Discov. 2019;18(3):175–96. https://doi.org/10.1038/s41573-018-0006-z.

38. Hause RJ, Pritchard CC, Shendure J, Salipante SJ. Classification and characterization of microsatellite instability across 18 cancer types. Nat Med. 2016;22(11):1342–50. https://doi.org/10.1038/nm.4191.
39. Diagnosis T, Guidelines For Colorectal Cancer Working Group C. Chinese Society of Clinical Oncology (CSCO) diagnosis and treatment guidelines for colorectal cancer 2018 (English version). Chin J Cancer Res. 2019;31(1):117–34. https://doi.org/10.21147/j.issn.1000-9604.2019.01.07.
40. Popat S, Hubner R, Houlston RS. Systematic review of microsatellite instability and colorectal cancer prognosis. J Clin Oncol. 2005;23(3):609–18. https://doi.org/10.1200/jco.2005.01.086.
41. Choi YY, Kim H, Shin SJ, Kim HY, Lee J, Yang HK et al. Microsatellite instability and Programmed Cell Death-Ligand 1 expression in stage II/III gastric Cancer: Post Hoc Analysis of the CLASSIC Randomized controlled study. *Ann Surg*. (2019);270(2):309–16. https://doi.org/10.1097/sla.0000000000002803
42. Le DT, Durham JN, Smith KN, Wang H, Bartlett BR, Aulakh LK, et al. Mismatch repair deficiency predicts response of solid tumors to PD-1 blockade. Science. 2017;357(6349):409–13. https://doi.org/10.1126/science.aan6733.
43. Addeo A, Friedlaender A, Banna GL, Weiss GJ. TMB or not TMB as a biomarker: that is the question. Crit Rev Oncol Hematol. 2021;163:103374. https://doi.org/10.1016/j.critrevonc.2021.103374.
44. Gan B. ACSL4, PUFA, and ferroptosis: new arsenal in anti-tumor immunity. Signal Transduct Target Ther. 2022;7(1):128. https://doi.org/10.1038/s41392-022-01004-z.
45. Lei G, Zhuang L, Gan B. Targeting ferroptosis as a vulnerability in cancer. Nat Rev Cancer. 2022;22(7):381–96. https://doi.org/10.1038/s41568-022-00459-0.
46. Chen X, Li J, Kang R, Klionsky DJ, Tang D. Ferroptosis: machinery and regulation. Autophagy. 2021;17(9):2054–81. https://doi.org/10.1080/15548627.2020.1810918.
47. Chen X, Kang R, Kroemer G, Tang D. Broadening horizons: the role of ferroptosis in cancer. Nat Rev Clin Oncol. 2021;18(5):280–96. https://doi.org/10.1038/s41571-020-00462-0.
48. Zhao L, Zhou X, Xie F, Zhang L, Yan H, Huang J, et al. Ferroptosis in cancer and cancer immunotherapy. Cancer Commun (Lond). 2022;42(2):88–116. https://doi.org/10.1002/cac2.12250.
49. Yi J, Zhu J, Wu J, Thompson CB, Jiang X. Oncogenic activation of PI3K-AKT-mTOR signaling suppresses ferroptosis via SREBP-mediated lipogenesis. Proc Natl Acad Sci U S A. 2020;117(49):31189–97. https://doi.org/10.1073/pnas.2017152117.
50. Ouyang S, Li H, Lou L, Huang Q, Zhang Z, Mo J, et al. Inhibition of STAT3-ferroptosis negative regulatory axis suppresses tumor growth and alleviates chemoresistance in gastric cancer. Redox Biol. 2022;52:102317. https://doi.org/10.1016/j.redox.2022.102317.
51. Xiao Y, Yu D. Tumor microenvironment as a therapeutic target in cancer. Pharmacol Ther. 2021;221:107753. https://doi.org/10.1016/j.pharmthera.2020.107753.
52. Niu X, Chen L, Li Y, Hu Z, He F. Ferroptosis, necroptosis, and pyroptosis in the tumor microenvironment: perspectives for immunotherapy of SCLC. Semin Cancer Biol. 2022;86(Pt 3):273–85. https://doi.org/10.1016/j.semcancer.2022.03.009.
53. Gajewski TF, Schreiber H, Fu YX. Innate and adaptive immune cells in the tumor microenvironment. Nat Immunol. 2013;14(10):1014–22. https://doi.org/10.1038/ni.2703.
54. Tanaka A, Sakaguchi S. Targeting Treg cells in cancer immunotherapy. Eur J Immunol. 2019;49(8):1140–6. https://doi.org/10.1002/eji.201847659.
55. Ku SC, Liu HL, Su CY, Yeh IJ, Yen MC, Anuraga G et al. Comprehensive analysis of prognostic significance of cadherin (CDH) gene family in breast cancer. *Aging (Albany NY)*. (2022);14(20):8498–567. https://doi.org/10.18632/aging.204357
56. Yu W, Yang L, Li T, Zhang Y. Cadherin signaling in Cancer: its functions and role as a therapeutic target. Front Oncol. 2019;9:989. https://doi.org/10.3389/fonc.2019.00989.
57. Lin WH, Cooper LM, Anastasiadis PZ. Cadherins and catenins in cancer: connecting cancer pathways and tumor microenvironment. Front Cell Dev Biol. 2023;11:1137013. https://doi.org/10.3389/fcell.2023.1137013.
58. Minikes AM, Song Y, Feng Y, Yoon C, Yoon SS, Jiang X. E-cadherin is a biomarker for ferroptosis sensitivity in diffuse gastric cancer. Oncogene. 2023;42(11):848–57. https://doi.org/10.1038/s41388-023-02599-5.
59. Chen X, Song X, Li J, Zhang R, Yu C, Zhou Z, et al. Identification of HPCAL1 as a specific autophagy receptor involved in ferroptosis. Autophagy. 2023;19(1):54–74. https://doi.org/10.1080/15548627.2022.2059170.
60. Xie J, Lan T, Zheng DL, Ding LC, Lu YG. CDH4 inhibits ferroptosis in oral squamous cell carcinoma cells. BMC Oral Health. 2023;23(1):329. https://doi.org/10.1186/s12903-023-03046-3.
61. Yu J, Sun X, Yu Y, Cui X. The cadherin protein CDH19 mediates cervical carcinoma progression by regulating AKT/NF-κB signaling. Acta Biochim Pol. 2023;70(4):955–61. https://doi.org/10.18388/abp.2020_6902.
62. Wang H, Liu J, Lou Y, Liu Y, Chen J, Liao X, et al. Identification and preliminary analysis of hub genes associated with bladder cancer progression by comprehensive bioinformatics analysis. Sci Rep. 2024;14(1):2782. https://doi.org/10.1038/s41598-024-53265-z.
63. Shi Y, Han T, Liu C. CircRNA hsa_circ_0006220 acts as a tumor suppressor gene by regulating miR-197-5p/CDH19 in triple-negative breast cancer. Ann Transl Med. 2021;9(15):1236. https://doi.org/10.21037/atm-21-2934.
64. Zhang W, Dai J, Hou G, Liu H, Zheng S, Wang X et al. SMURF2 predisposes cancer cell toward ferroptosis in GPX4-independent manners by promoting GSTP1 degradation. *Mol Cell*. (2023);83(23):4352–e698. https://doi.org/10.1016/j.molcel.2023.10.042
65. Yan X, Liu Y, Li C, Mao X, Xu T, Hu Z, et al. Pien-Tze-Huang prevents hepatocellular carcinoma by inducing ferroptosis via inhibiting SLC7A11-GSH-GPX4 axis. Cancer Cell Int. 2023;23(1):109. https://doi.org/10.1186/s12935-023-02946-2.
66. Dang R, Wang M, Li X, Wang H, Liu L, Wu Q, et al. Edaravone ameliorates depressive and anxiety-like behaviors via Sirt1/Nrf2/HO-1/Gpx4 pathway. J Neuroinflammation. 2022;19(1):41. https://doi.org/10.1186/s12974-022-02400-6.
67. Chen Y, Mi Y, Zhang X, Ma Q, Song Y, Zhang L, et al. Dihydroartemisinin-induced unfolded protein response feedback attenuates ferroptosis via PERK/ATF4/HSPA5 pathway in glioma cells. J Exp Clin Cancer Res. 2019;38(1):402. https://doi.org/10.1186/s13046-019-1413-7.
68. Zhang Y, Swanda RV, Nie L, Liu X, Wang C, Lee H, et al. mTORC1 couples cyst(e)ine availability with GPX4 protein synthesis and ferroptosis regulation. Nat Commun. 2021;12(1):1589. https://doi.org/10.1038/s41467-021-21841-w.
69. Liu Y, Wan Y, Jiang Y, Zhang L, Cheng W. GPX4: the hub of lipid oxidation, ferroptosis, disease and treatment. Biochim Biophys Acta Rev Cancer. 2023;1878(3):188890. https://doi.org/10.1016/j.bbcan.2023.188890.

Publisher's note